

Automated Electrochemistry for Measuring the Temperature Dependence of Various Cell  
Parameters via A Custom Built Microcontroller-Based Potentiostat

A Thesis submitted in partial fulfillment of the requirements for the degree of Master of  
Science at George Mason University

by

Benjamin Canon  
Bachelor of Science  
George Mason University, 2018

Director: Abul Hussam, Professor  
Department of Chemistry & Biochemistry

Fall 2022  
George Mason University  
Fairfax, VA

Copyright 2022 Benjamin Canon  
All Rights Reserved

## **DEDICATION**

I dedicate this work to my parents, Teresa and Jason Canon. It is their shoulders upon which I stand.

## ACKNOWLEDGEMENTS

I'd like to thank George Mason University for providing me a place in which to deepen my understanding and appreciation for our theories of the universe. I am gracious to both BluePath Labs and the U.S. Department of Homeland Security for contributing financially to my continued education. I'd also like to thank my committee for their role in this work. In particular, I want to acknowledge Dr. Abul Hussam, who has re-sparked my interest in the fusion of electronics and chemistry. Lastly, I'd like to give special thanks to Krysalyn Gerhardt for her support through this journey.

## TABLE OF CONTENTS

|                                                                                                                                             | Page |
|---------------------------------------------------------------------------------------------------------------------------------------------|------|
| List of Tables .....                                                                                                                        | vii  |
| List of Figures .....                                                                                                                       | viii |
| Abstract .....                                                                                                                              | ix   |
| Chapter 1: Introduction .....                                                                                                               | 1    |
| Section 1.1: Overview .....                                                                                                                 | 1    |
| Section 1.2: Prior Work .....                                                                                                               | 2    |
| Section 1.3: The Arduino's Construction .....                                                                                               | 3    |
| Section 1.4: Potentiostat Design .....                                                                                                      | 4    |
| Section 1.5: Digital Thermometers .....                                                                                                     | 6    |
| Section 1.6: Chronoamperometry and Chronocoulometry .....                                                                                   | 6    |
| Chapter 2: Potentiostat design, fabrication, and programming .....                                                                          | 10   |
| Section 2.1: Circuit Design and Component Choice .....                                                                                      | 10   |
| Section 2.2: Thermometer Design .....                                                                                                       | 12   |
| Section 2.3: PCB Design and Fabrication .....                                                                                               | 12   |
| Section 2.4: Potential Design Improvements .....                                                                                            | 14   |
| Section 2.5: Programming .....                                                                                                              | 15   |
| Chapter 3: Calibration and Characterization .....                                                                                           | 17   |
| Section 3.1: Voltage Source Calibration .....                                                                                               | 17   |
| Section 3.2: Determination of Noise Present in ADC Signal .....                                                                             | 20   |
| Section 3.3: Board Validation .....                                                                                                         | 21   |
| Section 3.4: Calibrating the Thermometer .....                                                                                              | 25   |
| Chapter 4: Chronoamperometry of Ferricyanide Under Diffusion Control .....                                                                  | 27   |
| Section 4.1: Cyclic Voltammetry .....                                                                                                       | 27   |
| Section 4.2 Measurement of the Capacitive Background .....                                                                                  | 29   |
| Section 4.3 Chronoamperometry of Ferricyanide Under Kinetic Control .....                                                                   | 33   |
| Section 4.4 Determination of Heterogenous Electron Transfer Rate Constants, Electron Transfer Activation Energy, and Frequency Factor ..... | 36   |
| Chapter 5: Chronoamperometry of POTASSIUM Ferricyanide Under Diffusion Control .....                                                        | 38   |

|                                                                                                        |    |
|--------------------------------------------------------------------------------------------------------|----|
| Section 5.1 Measurement of the Capacitive Background .....                                             | 38 |
| Section 5.2 Chronoamperometry of Potassium Ferricyanide Under Diffusion<br>Controlled Conditions ..... | 41 |
| Section 5.3 Determination of Diffusion Coefficients and Ionic Mobility.....                            | 43 |
| Section 5.4 Analysis of the Reverse Pulse and Measurement of Surface Excess.....                       | 46 |
| Chapter 6: Conclusions .....                                                                           | 50 |
| Section 6.1 Design Successes and Potential Improvements .....                                          | 50 |
| Section 6.2 Potentiostat Performance.....                                                              | 51 |
| Section 6.3 Temperature Dependent Electrochemistry .....                                               | 51 |
| Appendix.....                                                                                          | 53 |
| A.1 Potentiostat Schematic .....                                                                       | 54 |
| A.2 Cost Breakdown .....                                                                               | 55 |
| A.3 KiCad Component Schematic .....                                                                    | 56 |
| A.4 KiCad PCB Layout.....                                                                              | 57 |
| A.5 Potentiostat Shield.....                                                                           | 59 |
| References.....                                                                                        | 60 |

## LIST OF TABLES

| Table                                                                                                                                                                            | Page |
|----------------------------------------------------------------------------------------------------------------------------------------------------------------------------------|------|
| Table 1 Second Degree Polynomial Regression Results for Thermometer. Extra significant figures in errors are retained for error propagation calculations. Show the equation..... | 26   |
| Table 2 LINEST results from Aoki plot. ....                                                                                                                                      | 32   |
| Table 3 Results for k at each Temperature. ....                                                                                                                                  | 37   |
| Table 4 Regression Results from 400 mV to -200 mV Aoki Plot .....                                                                                                                | 40   |
| Table 5 Calculated Diffusion Coefficients .....                                                                                                                                  | 44   |
| Table 6 Diffusion Constants from Reverse Pulse .....                                                                                                                             | 47   |

## LIST OF FIGURES

| Figure                                                                                                       | Page |
|--------------------------------------------------------------------------------------------------------------|------|
| Figure 1. General Schematic for a 3-Electrode System with Potentiostat .....                                 | 5    |
| Figure 2 Calibration Curve for the Voltage Source .....                                                      | 18   |
| Figure 3 Noise Present in the Voltage Source .....                                                           | 19   |
| Figure 4 Plot of Log(SNR) vs. Current.....                                                                   | 21   |
| Figure 5 Cyclic Voltammetry on a 1k $\Omega$ Resistor. ....                                                  | 22   |
| Figure 6 Cyclic Voltammetry on a 150 $\mu$ F Capacitor .....                                                 | 23   |
| Figure 7 Chronoamperogram of an RC circuit. ....                                                             | 24   |
| Figure 8 Linearized RC Chronoamperogram .....                                                                | 25   |
| Figure 9 Temperature Calibration Curve.....                                                                  | 26   |
| Figure 10 Cyclic Voltammogram of 2.98 mM Potassium Ferricyanide.....                                         | 29   |
| Figure 11 Chronoamperograms of KCl. 400 mV to 200 mV pulse.....                                              | 30   |
| Figure 12 Aoki Plots for 200mV Pulse at Each Temperature .....                                               | 32   |
| Figure 13 KCl background subtracted Chronoamperograms of Potassium Ferricyanide Under Kinetic Control: ..... | 34   |
| Figure 14 Chronocoulograms of Potassium Ferricyanide Under Kinetic Control. ....                             | 35   |
| Figure 15 Q vs $t^{1/2}$ at Various Temperatures from Kinetics Data. ....                                    | 36   |
| Figure 16 Arrhenius Plot.....                                                                                | 37   |
| Figure 17 Chronoamperograms of aqueous KCl. Pulse: 400 mV to -200 mV vs. SSC ...                             | 39   |
| Figure 18 Aoki Plots. KCl 400 mV to -200 mV .....                                                            | 40   |
| Figure 19 $C_1$ vs T at Different Potential Steps.....                                                       | 41   |
| Figure 20 Chronoamperograms of Potassium Ferricyanide Under Diffusion Control.....                           | 42   |
| Figure 21 Chronocoulograms of Ferricyanide Under Diffusion Control .....                                     | 42   |
| Figure 22 Cottrell Plots of Potassium Ferricyanide. Forward Pulse: 400 to -200 mV vs. SSC .....              | 43   |
| Figure 23 Linear Regression of D vs. T.....                                                                  | 44   |
| Figure 24 Arrhenius plot for the Diffusion of Ferricyanide .....                                             | 45   |
| Figure 25 Linearized Reverse Pulse for Ferricyanide Under Diffusion Control .....                            | 46   |
| Figure 26 D vs. T. Reverse Pulse.....                                                                        | 47   |
| Figure 27 Reverse Pulse Arrhenius Plot for Diffusion. ....                                                   | 48   |
| Figure 28 $\Gamma_O - \Gamma_R$ as a function of Temperature. ....                                           | 49   |

## **ABSTRACT**

### **AUTOMATED ELECTROCHEMISTRY FOR MEASURING THE TEMPERATURE DEPENDENCE OF VARIOUS CELL PARAMETERS VIA A CUSTOM BUILT MICROCONTROLLER-BASED POTENTIOSTAT**

Benjamin Canon, M.S.

George Mason University, 2022

Thesis Director: Dr. Abul Hussam

A \$70 microcontroller based potentiostat with a temperature probe was designed, fabricated, and tested. The potentiostat was programmed to automatically repeat chronoamperometric experiments on a solution of potassium ferricyanide in potassium chloride at different temperatures under both kinetic and diffusion controlled conditions. Under kinetic control, the system proved to be quasi-reversible. Cottrellian behavior was observed under diffusion control. Currents due to the formation of an electric double layer were found to follow a power law. The temperature dependence of the heterogeneous rate constant, diffusion coefficient, double layer capacitance, and surface excess were all measured. From this data, the ionic mobility, activation energy and frequency factor for diffusion and heterogeneous electron transfer were all measured.

## CHAPTER 1: INTRODUCTION

### SECTION 1.1: OVERVIEW

With the advent of inexpensive microcontrollers, it is becoming increasingly common for students, researchers, and hobbyists alike to develop their own instrumentation. The motivation for this is easily understood. The student that builds and programs their own pH meter develops a deeper understanding of the instrument while gaining experience with both hardware and software – skills increasingly more important in the modern scientific world. The hobbyist gains access to instrumentation that is often otherwise prohibitively expensive. The researcher can automate tedious processes, allowing for higher scientific throughput. This trend is also fueled by the ever-growing repository of open-source software and designs.

A giant in the world of do-it-yourself automation is the Arduino Uno microcontroller. These programmable circuit boards are inexpensive (~\$10 USD) and allow users to control the behavior of customized systems easily via a computer. In chemistry, the Arduino microcontroller has been used to create instrumentation including Bluetooth pH meters<sup>1</sup>, uniaxial tensile testers<sup>2</sup>, fluorometers<sup>3</sup>, and even electrochemical scanning microscopes<sup>4</sup>. Such instruments are generally extremely low cost when compared to commercially available versions. Naturally, this brings into question their quality. While it's true that many of these microcontroller-based instruments should be confined to

educational applications, some are still good enough to find potential use in field work or in developing proofs-of-concept. Furthermore, the freedom to tailor an instrument to a specific application is highly desirable. For example, it would be useful to be able to automatically study electrochemical systems at a variety of temperatures. While many potentiostats come equipped with a temperature sensor, they are not designed to automatically repeat experiments at multiple temperatures. Rather, an analyst must be present to adjust the temperature and initialize the experiments. Most electrochemical systems do not have readily available temperature dependent data, at least in part, due to this inconvenience. A significant amount of information about how any system works can be gained from how its behavior changes with temperature, so herein is described the design, fabrication, and testing of a microcontroller-based potentiostat that can automatically perform electroanalytical experiments at different temperatures.

## **SECTION 1.2: PRIOR WORK**

There have been several successful attempts to design low cost potentiostats<sup>5-9</sup>. Brown developed an impressive open source potentiostat that is compatible with Android phones. Li has developed a kit that students can put together as part of an experiment to further student understanding. Meloni fabricated a basic printed circuit board (PCB) that can be mounted on top of an Arduino Uno; such PCBs are often called Arduino shields. There have been several others made, and they all apparently work quite well when used as designed. However, as general use potentiostats, they fall short in a few ways. First, they are limited in the potential ranges they can achieve, with most being less than  $\pm 2$  V. Exceptions to this, such as the Rodeostat, do not have very high-resolution control over the

potential. Another issue is limited current ranges. Electrochemical experiments involve current measurements that can span 9 orders of magnitude. Typically, current ranges in these low-cost potentiostats span only 3 orders of magnitude. Finally, scan rates are universally slow, the highest being 1 V/s. While microcontrollers are not designed for incredible speed, careful design should increase this specification.

### **SECTION 1.3: THE ARDUINO'S CONSTRUCTION**

An Arduino Uno board is driven using the ATmega328P microchip and contains all the necessary supporting hardware to make it function. The ATmega328P is made up of several different parts. It contains an erasable programmable read-only memory (EPROM) section, which allows the microchip to store and run small computer programs. Programs are easily written in the company's open-source integrated development environment (IDE). The language used within the IDE is built on top of the C++ programming language. New programs are uploaded to the microchip via a USB connection found on the Arduino board. This USB connection also allows for runtime communication between the microcontroller and the IDE, providing I/O capability.

The ATmega328P also comes equipped with a full-duplex serial peripheral interface (SPI). Many useful digital integrated circuit (IC) chips can be controlled at high speeds using SPI, and this gives the board a lot of functionality. Such interfaces generally consist of three types of signals: select signals, clock signals, and serial data signals. Data signals can be either input (from chip to Arduino) or output (from Arduino to chip). On the Arduino Uno, the data-out and data-in lines are distinct. This is common, and it allows for both input and output processes to occur simultaneously. The clock signal is responsible

for ensuring synchronous data transmission. Because the clock and data signals are typically shared among multiple chips, select signals are needed to manage when a given chip is communicating with the Arduino.

The last section of the chip we are interested in is an internal 10-bit analog-to-digital converter (ADC). This ADC can read voltages from 0 to 5 volts and convert them into a binary number ranging from 0 to  $2^{10}$ , giving  $\sim 5$  mV resolution. It is by using these features of the chip that the Arduino can be used to drive a wide variety of things such as robots, laboratory instrumentation, household security systems, and other embedded systems.\* Limitations of Arduino (10 bit ADC and real DAC) led us to design our own system with 16 bit fast ADC and DAC integrated with the potentiostat as described later.

#### **SECTION 1.4: POTENTIOSTAT DESIGN**

Potentiostats are control devices designed to investigate the properties of electrochemical systems. A common example of such a system is the three-electrode electrochemical cell, depicted below in Figure 1. Using a potentiostat, the voltage between the working and reference electrode is set. The current flowing between the working and

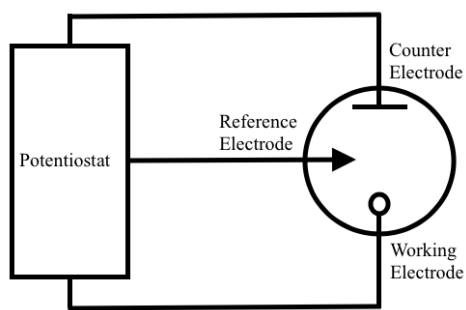


**Figure 1. General Schematic for a 3-Electrode System with Potentiostat**

counter electrodes is concurrently measured. While the three-electrode set up is common, a two-electrode variation may also be employed with the counter and reference electrodes shorted together.

Potentiostats can be thought of as consisting of three main parts: a voltage source, a current source, and an ammeter. The voltage source is used to fix the electrical potential between the reference and counter electrodes. This induces an electrical current between the electrodes. A digital-to-analog converter (DAC) allows for control of the voltage source; a computer sends a binary number to a DAC. The DAC then outputs a corresponding potential. This potential can then be amplified and buffered to provide access to larger potential ranges.

For the reference electrode to remain in a standard thermodynamic state, the net current flowing to or from it must be maintained at zero. The current source accomplishes this using a summing amplifier that adjusts the voltage between the counter and reference electrodes such that the current flowing from the counter to the reference is equal to that flowing from reference to working. Adjustment is automatic because the path from the

counter to reference electrode acts as a feedback loop for the amplifier.

Finally, the current flowing into or out of the working electrode is measured using the ammeter. An amplifier can be used as a current-to-voltage converter (CVC). Such amplifiers in commercially available potentiostats have different gain settings so that currents of many orders of magnitude can be mapped onto a comparatively smaller potential range. The output potential of the CVC can then finally be converted to a binary number using an analog-to-digital converter (ADC), whose output is ultimately read by a computer.

### **SECTION 1.5: DIGITAL THERMOMETERS**

Digital thermometers can range in complexity, but a common design is a simple voltage divider comprised of a resistor and thermistor. A constant potential is applied across the divider. As the resistance of the thermistor varies from changes in temperature, so does the fraction of the voltage across it. The potential in the middle of the divider  $V_T$  is then dependent on temperature and can be used as a thermometer.

In general, the resistance of the thermistor follows the form of the Steinhart-Hart equation, seen below as Equation 1. The constants  $a$ ,  $b$ , and  $c$  are easily obtained through regression. However, in this use-case, it can be easier to simply perform polynomial regression on  $V_T$  data taken at multiple temperatures over the desired range.

$$\frac{1}{T} = a + b\ln(R) + c\ln(R)^3 \quad (1)$$

### **SECTION 1.6: CHRONOAMPEROMETRY AND CHRONOCOULOMETRY**

There are many types of electroanalytical analysis that one can perform on a cell.

Of primary interest here is a class of experiments called *double pulse chronoamperometry* (DPCA). Currents in an electrochemical system can either be Faradaic or non-Faradaic. Faradaic currents occur when the cell is set at a potential that can drive an electrochemical reaction. Non-Faradaic currents are capacitive, arising due to the formation of an electric double-layer close to the interface between an electrode and the solution in which it is submerged. These non-Faradaic currents are transient, decaying as the electric double layer becomes fully formed. In DPCA, a cell is initially maintained at a non-Faradaic potential for a period of time sufficient for transient currents to vanish, called the quiet time. The potential is then stepped to one under which electron transfer occurs, and the resulting Faradaic current is measured. This is called the forward pulse. Finally, the potential is stepped back to its original value, and again the current is measured. This is called the reverse pulse.

For large potential steps, the current eventually stabilizes to what is termed the *limiting current*. This is because once the electroactive species near the electrode is consumed, further reaction depends on the diffusion of additional ions through the solution. Under these conditions, the reaction is referred to as being *diffusion controlled*. The current as a function of time for a diffusion controlled forward pulse is given by the Cottrell equation, below as Equation 2<sup>10</sup>. If the bulk analyte concentration  $C_0$  and electrode area  $A$  are known, then this equation provides a convenient way to determine the diffusion coefficient of the analyte using DPCA.

$$i = \frac{nFA C_0 \sqrt{D_0}}{\sqrt{\pi t}} \quad (2)$$

It is common practice, however, to work with *chronocoulometric* data. Integration

significantly reduces noise; peaks and troughs work to negate one another. Integrating Equation 2 with respect to time yields Equation 3<sup>11</sup>.

$$Q = \frac{2nFAC_O\sqrt{D_O}}{\sqrt{\pi}}\sqrt{t} \quad (3)$$

Two additional sources of charge have to be considered. There is excess charge  $Q_{dl}$  that flows as the capacitive double-layer charges. This charge accumulates much more quickly than the time scales typical for DPCA and is therefore taken to be constant. Additionally, a small amount of electroactive species may be adsorbed onto the surface of the electrode. When the system is pulsed to a new potential, this adsorbed material reacts very quickly. The concentration (mole per unit area) of the adsorbed material is referred to as surface excess. The surface excess of the oxidized and reduced species are denoted  $\Gamma_O$  and  $\Gamma_R$  respectively. In general, the charge moved during the forward pulse is given by

$$Q = \frac{2nFAC_O\sqrt{D_O}}{\sqrt{\pi}}\sqrt{t} + Q_{dl} + nFA(\Gamma_O - \Gamma_R) \quad (4)$$

If after a time  $\tau$  a reverse pulse is applied, it can be shown that the resulting reversal charge is given by

$$Q_r(t > \tau) = \frac{2nFAC_O\sqrt{D_O}}{\sqrt{\pi}}\theta + Q_{dl} \quad (5)$$

where  $\theta = [\tau^{1/2} + (t - \tau)^{1/2} - t^{1/2}]$ . Note that the difference in the intercepts between Equations 4 and 5 is just  $nFA(\Gamma_O - \Gamma_R)$ . This holds as long as the final potential is the same as the initial, because the two  $Q_{dl}$  values are equal.

If DCPA experiments are performed at different temperatures, the observed diffusion constants should vary according to the Einstein-Smoluchowski equation,

$$D = \frac{\mu k_B T}{q} \quad (6)$$

where  $k_B$  is Boltzmann's constant,  $T$  is temperature,  $q$  is the charge of the electroactive species, and  $\mu$  is the ionic mobility. This equation provides a way to determine ionic mobility if diffusion constants are measured at different temperatures.

If a smaller potential step is used, bringing the potential closer to the cell's standard potential, the current will instead be limited by the kinetics of the heterogeneous electron transfer. Under these *kinetic controlled* conditions, the charge during the forward pulse as a function of time follows

$$Q = nFAkC_o \left( \frac{2\sqrt{t}}{H\sqrt{\pi}} - \frac{1}{H^2} \right); H = \frac{\sqrt{\pi}}{2t_i^{1/2}} \quad (7)$$

where  $t_i^{1/2}$  is the intercept of the data on the  $t^{1/2}$ -axis and  $k$  is the heterogeneous electron transfer rate constant. Equation 7 provides a simple method for measuring  $k$ . Longer pulse widths are desirable when using this method, because a more complex relationship is observed as  $t \rightarrow 0$ .

The dependence on the heterogeneous rate constant on temperature should be given by the Arrhenius equation, see Equation 8. Through this equation, measuring the rate constant at several temperatures enables one to determine both the activation energy  $E_a$  and frequency factor  $A$ .

$$k = Ae^{-\frac{E_a}{RT}} \quad (8)$$

## CHAPTER 2: POTENTIOSTAT DESIGN, FABRICATION, AND PROGRAMMING

### SECTION 2.1: CIRCUIT DESIGN AND COMPONENT CHOICE

The general design of a potentiostat is well documented, but implementations can vary. For this work, the circuit schematic (Section A.1) was heavily dependent on the choice of DAC and ADC. Amplifiers and filters beyond those used in the summing amplifier and CVC were added to produce stable, low-noise signals. A complete list of parts along with quantity and price can be found in Section A.2. All components were sourced from either Mouser or DigiKey. The open source software KiCad was used to generate a component schematic, which can be seen in Appendix C.

The DAC chosen was the AD5660. The AD5660 offers 16-bit resolution with a relative accuracy of  $\pm 1$  LSB. When run using a power supply of +5 V, the AD5660 provides an output potential range of 0 – 5 V, along with a buffered internal reference pin at 2.5 V. The AD5660 can be controlled using standard SPI with clock speeds up to 30 MHz, well beyond the capabilities of the Arduino Uno. The Arduino's own 5V was used to supply power to the chip. The DAC output  $V_{DO}$  and reference  $V_{DR}$  are not designed to be loaded, and therefore needed to be buffered. Thus,  $V_{DO}$  and  $V_{DR}$  were buffered through active low-pass and band-pass filters respectively.

The actively filtered DAC signals were then combined using a level shifting amplifier with a gain of two. The output  $V$  of this amplifier is given by

$$V = 2(V_{DO} - V_{DR}) \quad (9)$$

Plugging in the extrema for  $V_{DO}$  shows that  $V$  has a range of  $\pm 5$  V. Finally, the output of the level shifting amplifier is then buffered with a final active low-pass filter, creating a low-noise voltage source,  $V_s$ .

To prevent loading, the signal from the reference electrode was passed through a buffer amplifier. The buffered reference voltage and  $V_s$  were combined through the use of a summing amplifier. The output of the amplifier connects to the counter electrode. This has the effect of driving the potential of the reference electrode to  $-V_s$  with respect to ground. It is this summing amplifier that also acts as the current source to the counter electrode.

The working electrode connects to a virtual ground by way of an amplifier configured to be a CVC. An FST3125 4-bit digital switch was used to select between different gain levels for the current-to-voltage converter. This chip was chosen because of its claim to contribute very little noise as well as fast switching times (0.25 ns). The resulting voltage is then sent into an active low pass filter. A passive low pass filter is subsequently used to set the impedance of the signal and further reduce noise prior to being sent to the ADC.

The ADC used was a MAX11168. The MAX11168 is a 16-bit bipolar ADC with an input range from -5 to 5 V. It can be controlled using standard SPI protocols and is designed to operate at speeds of up to 500k samples per second. This chip is also powered using the +5 V from the Arduino. Setting the impedance of the input signal is necessary to ensure the ADC does not load the signal significantly. It also helps to ensure the signal noise does not

impact the accuracy of measurements.

Two TLC2247 quad op-amps were used to cover the amplification requirements of the circuit. One of the TLC2274 ICs was used in conjunction with the AD5560 to create the voltage source. The second TLC2274 provided the remaining four amplifiers. These amplifiers were chosen for their low input bias current of 1 pA. While this was not necessary for most of the amplifiers to have, it was desirable for the current to voltage converter. The offset voltage maximum for these amplifiers is 950  $\mu$ V.

The amplifiers all required a positive and negative power supply. In an effort to remove the need for external power, a PDM2-S5-D7-D voltage converter was used. This DC-DC converter is powered using the Arduino's +5 V supply, and outputs both +7 V and -7 V.

## **SECTION 2.2: THERMOMETER DESIGN**

The digital thermometer was of the simple design discussed in Section 1.4. A voltage divider comprised of a fixed resistor and a thermistor was implemented. The resistor was connected to ground, and the thermistor was connected to +5 V. The divided voltage was connected to one of the Arduino's analog read pins, which is read using the internal ADC of the ATmega328P.

## **SECTION 2.3: PCB DESIGN AND FABRICATION**

KiCad is an open source software package that enables users to design PCBs. Every electrical component was input into the software, and their connections designated to create a component schematic, which can be seen in Section A.4. Each component was then assigned a *footprint*. The footprints define how a particular component is mounted on the

PCB depending on its geometry, size, number of leads, etc. Since component shapes and sizes are standardized, KiCad provides a library of many common footprints. Customized footprints are easy to create, however, which was necessary for the PDM2-S5-D7-D voltage converter.

Once the component schematic was created, KiCad was then used to design the layout of the PCB. To reduce noise, large ground and power planes were used. Many of the other noise-reducing design choices came directly from recommendations found in the components' data sheets. For example, both 10  $\mu\text{F}$  and 0.1  $\mu\text{F}$  decoupling capacitors were placed as close as physically possible to the power pin of the DAC, in accordance with its data sheet. In addition, digital data lines were kept as far away as possible from analog lines when possible. A model of both the front and back of the PCB design is available in Appendix E. After the PCB design was complete, Gerber files were generated. This is a standard file format used by most PCB manufactures. The Gerber files were sent to JLPPCB (China) for manufacturing. Five boards were created along with a PCB stencil. A photo of the board can be seen in Section A.5.

Many of the components used were quite small (0201 package). Conventional wire solder is impractical to mount such components, and solder paste is typically used. Stencils provide a way to apply the solder paste more quickly. These are thin metal sheets with holes cut in such a way that they line up with the solder pads found on the PCB. Solder paste can be squeezed onto the pads. It was ultimately determined, though, that the stencil was not needed because of the relatively low number of components. Solder paste was simply applied to the component pads using fine tip tweezers. Pre-heating the board using

a heat gun made this process easier, as it enabled the paste to cling more easily to the pads. All surface mount components were then put into place, and a heat gun was used to melt the solder paste. Through-hole components were soldered using normal wire solder and a fine tip soldering iron. Electrical connections were verified using the short-circuit detection setting on a RadioShack True RMS Digital Multimeter (USA).

#### **SECTION 2.4: POTENTIAL DESIGN IMPROVEMENTS**

The TLC2774s were selected because of their low bias current, but their absolute maximum power supply rating is 16 V differential. This makes it impossible to create a -5 to 5 V range for the voltage source in a three-electrode configuration. A more realistic range is -3.3 to +3.3 V. With the reference and counter electrodes connected, however, the range is expanded to the desired -5 to +5 V. Switching to amplifiers that can handle higher supply voltages has the downside of usually increasing the bias current. A different DC-DC converter would also have to be used.

Rather than the FST3125, a 4-channel multiplexer should have been used to select between gain values. The FST3125 switches draw about 1  $\mu\text{A}$  in their high impedance state. This effectively acts as a  $\sim 2\text{M}\Omega$  resistor. Because all the gain resistors are in parallel, this destroys the functionality of the two highest gain settings (10M $\Omega$  and 1G $\Omega$ ). Multiplexers generally have significantly higher off-state impedances (often in the G $\Omega$  range).

Currently, the voltage source needs to be calibrated due to non-ideal behavior from the DAC and level shifting amplifier. The addition of a second ADC measuring the potential between the reference and working electrodes would likely eliminate the need for

manual calibration. If a switch was added before the counter electrode, this would also enable the measurement of open-circuit potentials.

It is well known that printing data to a screen is generally a very slow process compared to calculations. Due to the limited memory of the Arduino, data must be printed to the screen as it is collected. The addition of an SPI controlled flash memory chip would eliminate this need, and greatly increase ramp rates by allowing data to be printed to the screen after an experiment is done.

## **SECTION 2.5: PROGRAMMING**

Arduino programs are written in the C++ programming language. As such, the code was organized into four libraries, each consisting of a header and source file. The four libraries contain instructions for 1) controlling the ADC, 2) controlling the DAC, 3) controlling the thermometer, and 4) performing different types of experiments such as chronoamperometry and cyclic voltammetry.

The ADC library contains five functions. The first, `init_ADC(void)`, simply is used to initialize the Arduino pins to their default state upon powering up. Another, `p_read(void)`, reads the potential at the input pin of the ADC by calling SPI functions native to the Arduino. The data sheet for the ADC specifies that a certain sampling rate must be maintained for accurate measurement, so a single `p_read(void)` call is not sufficient. Thus, `p_read_ave(int count)` was included, which takes a total of  $(count + 10)$  readings; the first and final five measurements are ignored, and the remaining count measurements are averaged. Each call to `p_read(void)` takes approximately 8  $\mu$ s. Count values up to 100 add negligible time, but not much improvement in the signal-to-noise ratio (SNR) is seen above

25. The remaining two functions simply increase or decrease the gain by controlling the FST3125 switch.

The DAC library contains two functions. The first, `init_DAC(void)` initializes the Arduino pins needed for control of the DAC, similar to `init_ADC(void)`. The second, `p_write(double potential)`, takes in the desired output potential of the voltage source and writes the value to the DAC that is required to achieve that potential.

The thermometer library also contains just two functions. The Arduino pin necessary for reading the voltage across the standard resistor is set by `init_thermometer(void)`. Measurements are made using `get_temp(void)`.

The final library contains a list of various routines that combine these resources to perform electrochemical experiments. Currently, there is no interface that allows for runtime selection of which routines should be run and under which parameters. Rather, the source code is updated and re-uploaded to the Arduino. It is the intention of the author to develop graphical user interface to allow for easier control of the potentiostat.

## **CHAPTER 3: CALIBRATION AND CHARACTERIZATION**

### **SECTION 3.1: VOLTAGE SOURCE CALIBRATION**

The output of the voltage source strays from ideal behavior due to non-ideal characteristics of the DAC as well as the various amplifiers. Errors in the DAC zero-code, DAC linearity, gain resistances, and offset potentials all combine to create an offset zero point as well as non-unity slope in the voltage source, thus making calibration necessary. To achieve this, the voltage source was programmatically set at several voltages and the actual voltage was measured using the RadioShack multimeter. A correction curve was then determined through linear regression. This correction curve was included in the source code to ensure the voltage source output was accurate. It is important to note that this process needed to be repeated for each circuit board. The results from moving the voltage source from -2.500 V to 2.500 V in 0.100 V increments are shown in Figure 2.

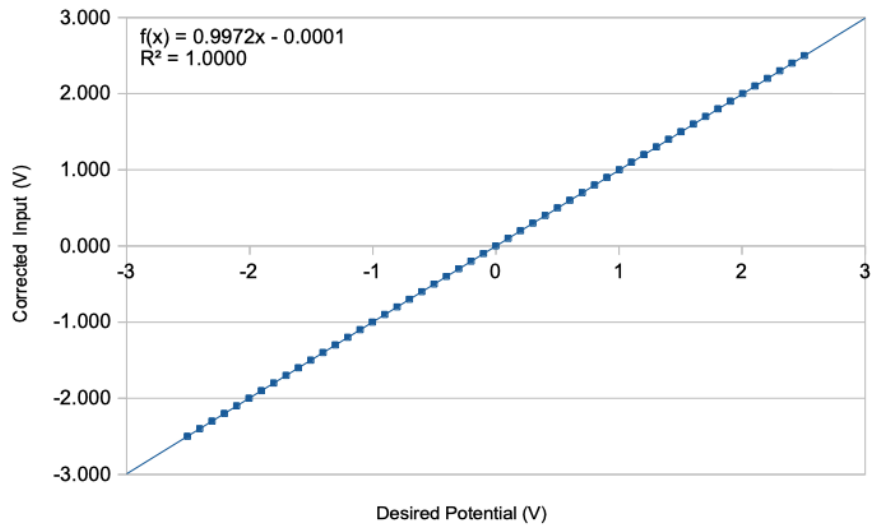


**Figure 2 Calibration Curve for the Voltage Source; -2.5 to 2.5 V; 0.1 V Increments.**

Strong linearity is observed. The linear regression is given below as Equation 10. Before writing a value to the DAC, `p_write(void)` must make adjustments using this equation so that the output potential is correct.

$$V_{Corrected} = 0.99719 \pm 0.00004V_{Desired} - 0.00123 \pm 0.00006 \quad (10)$$

A calibration curve like this was used during the remaining experiments discussed herein. As one would expect, the relative error in the voltage source increases as the magnitude of the potential decreases. The accuracy of the intervals between steps stays high, however. For example, if 1.500 V is requested, 1.498 V is output. Increasing to 1.501 V results in an output of 1.499 V, accurately 1 mV higher. If 250 mV is requested, 246 mV is output. Increasing to 251 mV results in an output of 247 mV, still accurately 1 mV higher.

A second more effective calibration method was discovered after experimentation was complete. The process is analogous to calibrating a pH meter. Set the slope and

intercept in the correction step of the code to 1.000 and 0.000 respectively. Set the desired potential to 0.000 V. The negative of the resulting potential can be used at the intercept. Then, set the desired potential high, 4.500 V was used. Adjust the slope of the correction manually until the actual potential matches. This method allows for  $\pm 0.5$  mV accuracy.

The noise present in the voltage source was measured using an LabNation Smart Scope. The readout can be seen in Figure 3. An apparent decaying ripple with an initial amplitude of  $\sim 75$  mV at a frequency of  $\sim 333$  kHz occurs every  $3.1 \mu\text{s}$ . The source of this ripple appears to be the TLC2774 amplifiers. Measurements of the Arduino power, the output put of the PDM2-S5-D7-D converter, the DAC reference, and DAC signal pins do not show this ripple. The ripple is high enough frequency to likely be unimportant on the measurement time scales available to the Arduino, though, and is seemingly averaged out.

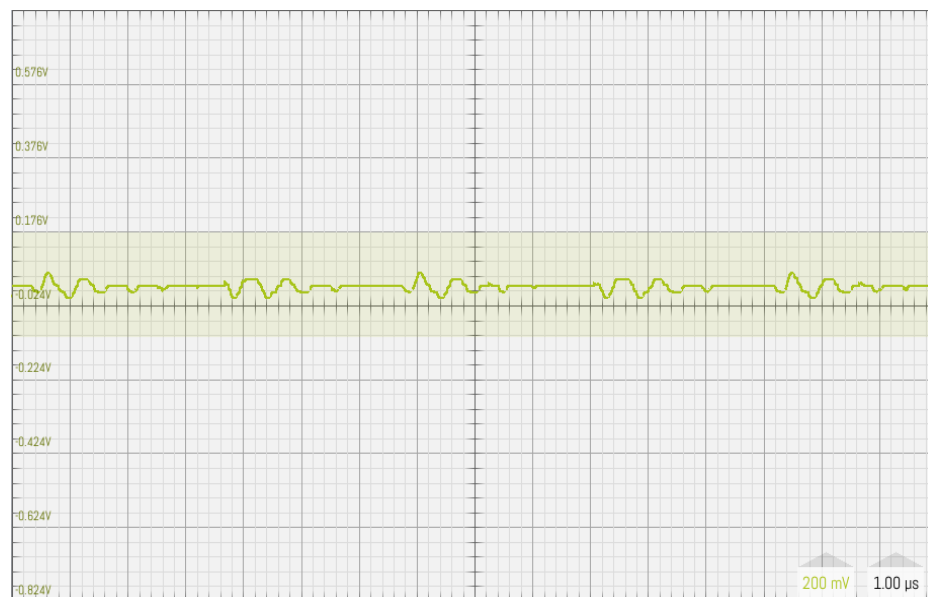


**Figure 3 Noise Present in the Voltage Source Captured Using a LabNation SmartScope.**

### SECTION 3.2: DETERMINATION OF NOISE PRESENT IN ADC SIGNAL

To determine the noise level present in measurements made by the ADC, the potentiostat was connected to a  $1\text{k}\Omega$  resistor in a two-electrode configuration (reference and counter electrodes connected together). The voltage was set to potentials ranging from  $-2.500\text{ V}$  to  $2.500\text{ V}$  in  $0.100\text{ V}$  increments. The resulting current through the resistor was measured 100 times with an averaging count of 5 (see Section 2.5 on programming). Both the average and standard deviation for each set of data was calculated, and their ratio determined. This was taken to be the SNR. Figure 4 is a plot of  $\log_{10}(\text{SNR})$  vs. current on the lowest gain setting. The minimum corresponds to a SNR of  $\sim 30$  at a current of  $\sim 7\ \mu\text{A}$ . The noise level remained constant across the different current measurements at  $0.22 \pm 0.03\ \mu\text{A}$ . A common rule of thumb is that the smallest measurable signal is three times the SNR. This should mean that currents down to about  $0.7\ \mu\text{A}$  can be accurately measured with this gain setting. The higher gain setting of 100k exhibits similar behavior, but with currents smaller by a factor of 100 or  $70\ \text{nA}$ .

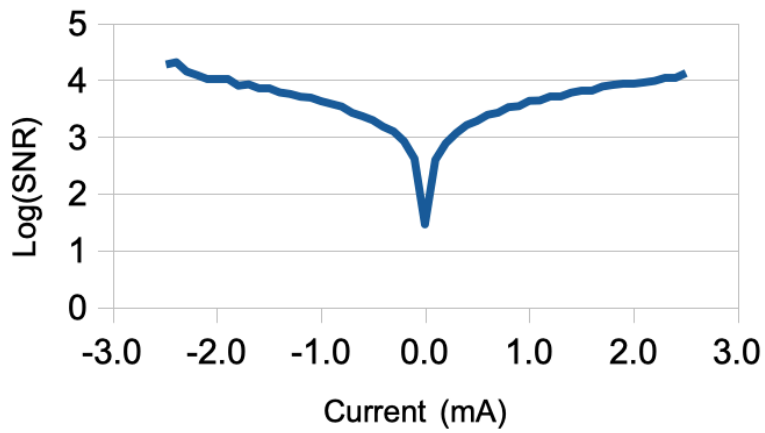


Figure 4 Plot of Log(SNR) vs. Current at a CVC gain setting of 1000.

### SECTION 3.3: BOARD VALIDATION

To check the validity of the board, several dummy cells were tested. To ensure baseline functionality, the cyclic voltammogram of a resistor was measured. The results are shown in Figure 5. The slope of this line should be the reciprocal of the value of resistance. Taking the reciprocal of the slope gives a value of  $1.002 \pm 0.000$  k $\Omega$ . The value measured by the RadioShack multimeter was  $0.999 \pm 0.005$  k $\Omega$ , making the two measurements in excellent agreement.

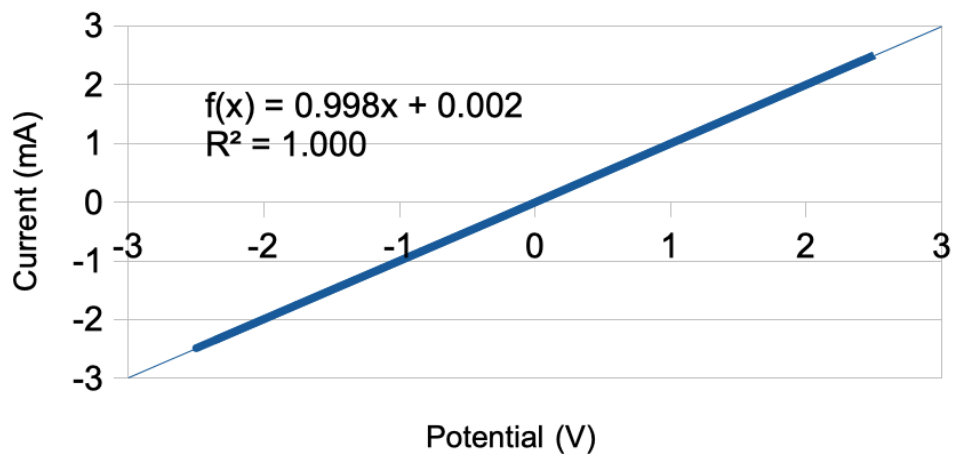


Figure 5 Cyclic Voltammetry on a  $1\text{k}\Omega$  Resistor. Gain = 1000

Next, a cyclic voltammetry was performed on a  $150\ \mu\text{F}$  electrolytic capacitor. Because the effective series resistance of capacitors is very small, the current should be approximately constant according to the equation

$$i = vC \quad (11)$$

where  $v$  is the ramp rate. Figure 6 shows the results taken at a ramp rate of  $0.858\ \text{V/s}$ . When the potential was increasing, the current was a constant  $177 \pm 2\ \mu\text{A}$ . As the potential was decreasing, the current was likewise constant at  $-178 \pm 1\ \mu\text{A}$ . When the magnitude of these is averaged and multiplied by the ramp rate, a value of  $152 \pm 2\ \mu\text{F}$  is obtained. The capacitor was unfortunately outside of the range of the RadioShack multimeter, but this was considered sufficient evidence for valid behavior.

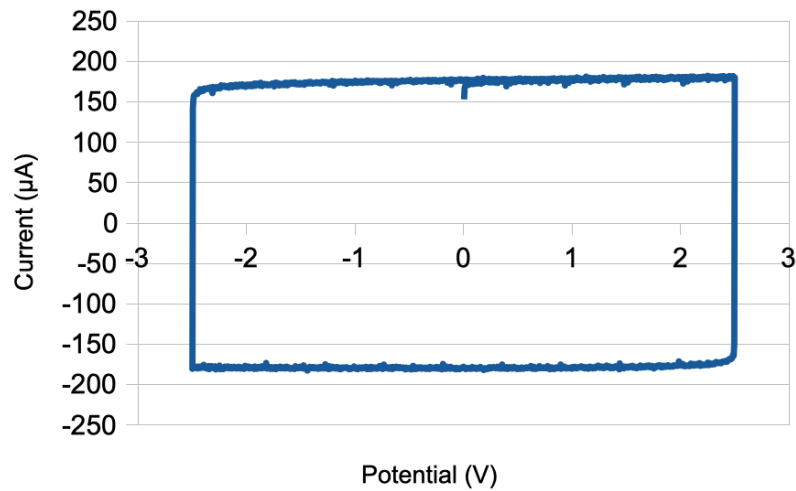


Figure 6 Cyclic Voltammetry on a 150  $\mu\text{F}$  Capacitor. Ramp Rate = 0.858 V/s.

Finally, an RC circuit comprised of a 1 k $\Omega$  resistor and 33  $\mu\text{F}$  capacitor was tested using a potential pulse experiment. The circuit was kept at 400 mV for 5000 ms to allow for transients to vanish. The potential was pulsed to 200 mV for 800 ms and then back to 400 mV while the resulting current was read at a sampling rate of 178 samples/s. The chronoamperogram is shown below in Figure 7. It should be noted that conventional current was positive in this case.

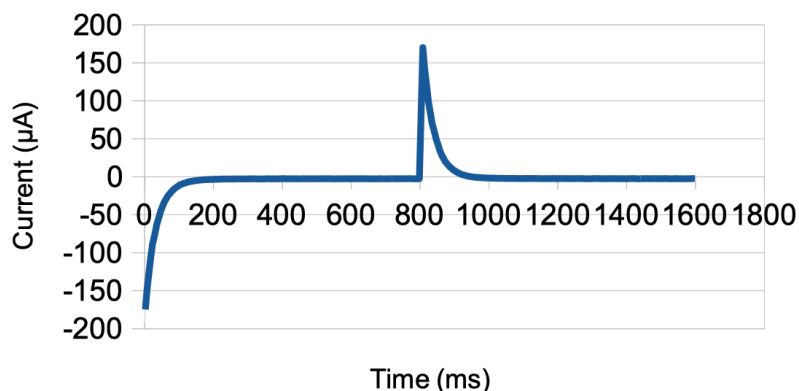


Figure 7 Chronoamperogram of an RC circuit. 400 mV → 200 mV. Sampling Rate = 178 Samples/s

The natural log of current should be linear with time according to Equation 12 below. To determine the time constant of the circuit, the natural log of current for the forward pulse is plotted as a function of time, which can be seen in Figure 8. Only the initial data is plotted. It deviates from ideality at time increases. The slope was determined to be  $-0.0306 \pm 0.0005 \mu\text{s}^{-1}$ . The reciprocal gives a time constant of  $32.6 \pm 0.6 \mu\text{s}$ . The resistance and capacitance measured via the RadioShack multimeter were  $1000 \pm 5 \Omega$  and  $31.9 \pm 0.4 \mu\text{F}$  respectively. Multiplying these yields a time constant of  $31.9 \pm 0.2 \mu\text{s}$ , in reasonable agreement with that measured via the potentiostat.

$$\ln(i) = -\frac{1}{RC}t + \ln\left(\frac{V}{R}\right) \quad (12)$$

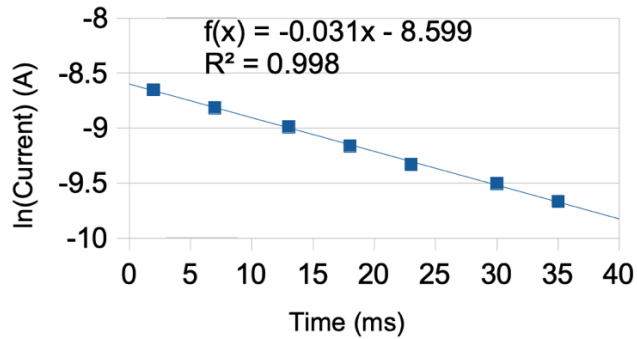
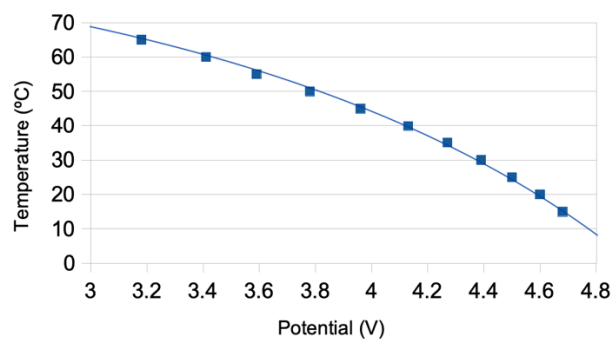


Figure 8 Linearized RC Chronoamperogram

### SECTION 3.4: CALIBRATING THE THERMOMETER

The resistance of a thermistor varies with temperature in accordance with the Steinhart-Hart equation. It is not necessary, however, to fit data to this model. The thermistor is part of a simple voltage divider. Measuring the voltage at the center of the divider as a function of temperature provides a sufficient calibration curve using polynomial fitting. A Haake (USA) recirculating thermostat bath was adjusted to temperatures from 15°C to 65°C in 5° intervals with the thermistor submerged. The resulting voltage was recorded. The data is shown graphically below in Figure 9.



**Figure 9 Temperature Calibration Curve.**

Through second order polynomial fitting the table below was obtained. The calibration has an  $R^2 = 0.998$  and provides degree accuracy ( $\pm 0.8^\circ\text{C}$ ).

**Table 1 Second Degree Polynomial Regression Results for Thermometer. Extra significant figures in errors are retained for error propagation calculations. Show the equation**

| <b>Parameter</b> | <b><math>V^2</math></b> | <b><math>V</math></b>   | <b><math>b</math></b> |
|------------------|-------------------------|-------------------------|-----------------------|
| <b>Value</b>     | -10.6425                | 51.6046                 | 7.8161                |
| $\pm$            | 1.252                   | 9.9237                  | 19.4278               |
|                  |                         | <b><math>R^2</math></b> | 0.998                 |

## CHAPTER 4: CHRONOAMPEROMETRY OF FERRICYANIDE UNDER DIFFUSION CONTROL

### SECTION 4.1: CYCLIC VOLTAMMETRY

A 2.98 mM solution of  $K_3Fe(CN)_6$  prepared in 0.1 M KCl. The solution was placed into a thermostated cell. A Haake recirculating bath was used to control the temperature of the cell. Rubber tubing insulated with foam connected the recirculating pump to the jacket inlet and outlet of the cell. The insulation was utilized to help ensure the cell temperature remained the same as the water bath throughout experimentation. The cell itself was insulated with aluminum foil. A 3.0 mm diameter glassy carbon electrode (GCE) was used for the working electrode. The surface of this electrode was periodically polished by wet sanding with 0.05  $\mu\text{m}$  alumina grit suspended in distilled water. A silver-silver chloride (SSC) standard electrode was used as the reference electrode. The counter electrode was a platinum wire. The solution was degassed with nitrogen gas for at least five minutes prior to all experiments. The purge tube was left at the top of the solution to prevent oxygen reentering the cell.

Cyclic voltammetry provides an easy way to determine the potentials at which potential a redox reaction will be controlled by the kinetics of electron transfer or by diffusion. Figure 10 shows the cyclic voltammogram of the ferricyanide solution at 25°C. Note that reduction current is taken as positive in all experiments performed on electrochemical cells. The potential was initially set to 0.400 V for a quiet time of 30

seconds. It was ramped down to -0.400 V and then back up to the initial potential at a ramping rate of 50 mV/s. Initially, no current flows because the potential is well above that required for reduction. There is, however, an offset from zero in the current measurement. This is from capacitive charging due to the potential step and from the zero-code offset present within the ADC. This background current value is much smaller than the redox current and generally subtracted from the redox currents. Current begins flowing near 225 mV and increases sharply until 125 mV. This region represents the potential region under which the reduction of ferricyanide is limited by the kinetics of the reaction. To perform kinetic controlled chronoamperometry, the potential would be initially held at 400 mV, then stepped to 200 mV. This is close to the standard redox potential (ca.  $E_{1/2}$ ) of the redox couple. Then, it would be stepped back to 400 mV for the reverse pulse. The current levels off after approximately -200 mV. This region represents potentials under which the reaction is diffusion controlled. To perform diffusion controlled chronoamperometry, the second potential would be set at -200 mV instead. The distortion of the voltammogram at -400 mV is likely due to a programming issue.

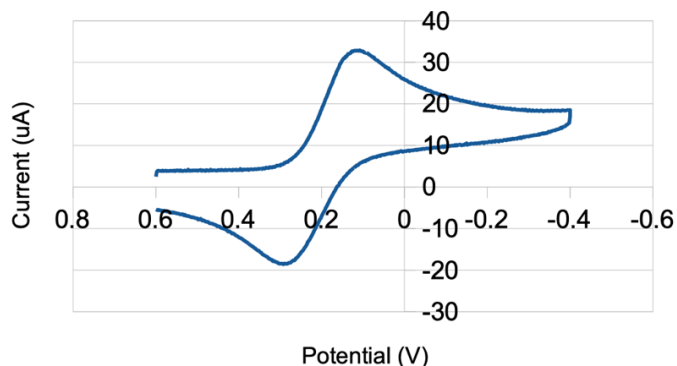


**Figure 10** Cyclic Voltammogram of 2.98 mM Potassium Ferricyanide in 0.1 M KCl. Signal shows without filtering.  $E_{1/2} = (E_{p, \text{cathodic}} + E_{p, \text{anodic}}) / 2 = 200 \text{ mV vs. SSC}$ . Scan Rate = 50 mV/s.

#### SECTION 4.2 MEASUREMENT OF THE CAPACITIVE BACKGROUND

The capacitive background of the 0.1M KCl solution was first measured under the same conditions that would be later used for both the diffusion and kinetic controlled experiments with ferricyanide. The cell was filled with the KCl solution. The Haake bath was initially set to 65.0°C. The bath was then set to 10°C. The potentiostat monitored the temperature of the cell as the bath cooled. At 5° intervals, two experiments were run: one using the smaller potential step from 400 mV to 200 mV, and another from 400 mV to -200 mV. It was more efficient to do this, and the temperature did not change significantly between experiments (~0.5°). A pulse width of 800 ms was used with a sampling rate of about 175 samples per second for both pulses. The quiet time was set to be 30 seconds. Data collected in response to the larger potential step will be discussed in Chapter 5. The capacitive chronoamperograms for the smaller potential step at each of the temperatures are shown in Figure 11. Higher currents result at higher temperatures. As temperature

increases, the viscosity, and thus the frictional drag on electrolyte ions, decreases. Ions also have more thermal energy to overcome this drag, leading to higher currents.

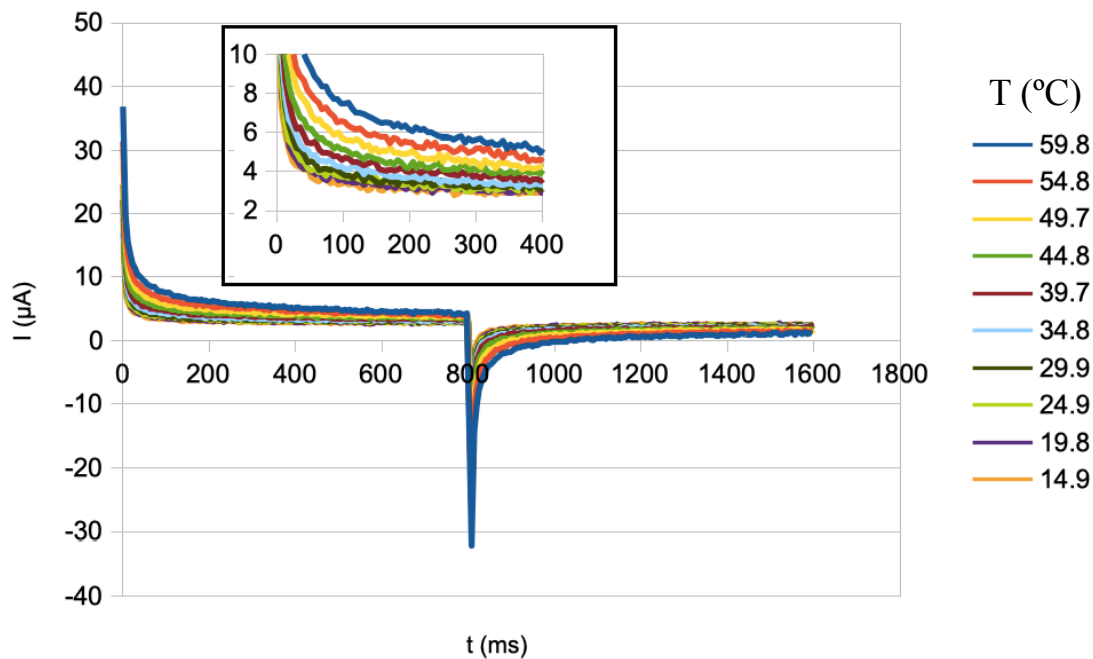


Figure 11 Chronoamperograms of KCl. 400 mV to 200 mV pulse. PW = 800 ms. SR = 175 samples/s. The expanded portion shows the change with temperature more clearly.

The noise present in each signal is more easily seen in the enlarged section at the top right of Figure 11. This noise is consistent with that discussed earlier (Gain = 1000), with a standard deviation of  $\sim 0.2 \mu\text{A}$ . While sufficient for this purpose, switching to a higher gain setting would improve the SNR. It is also notable that there appears to be an offset of about  $2 \mu\text{A}$ . This is likely a combination of the input offset voltage of the operational amplifiers as well as zero code error present in the ADC. This offset is small for the current range the gain setting was intended for (5 mA – 10  $\mu\text{A}$ ). It ultimately was

not necessary to correct for this; these backgrounds were to be subtracted from data collected from experiments with ferricyanide. Doing so removes the offset from the ferricyanide data as well.

It is often assumed that capacitive current decays exponentially. This stems from the assumption that double layer capacitance is constant. However, it takes a finite amount of time for dipoles present in solution to orient themselves with the electric field within the double-layer. This delay is referred to as dielectric excitation, and effectively makes the value for the double-layer capacitance time-dependent. It has been shown<sup>12</sup> that, when this is considered, current follows a power law. For a potential step of size  $\Delta V$ , the current is related to the elapsed time by

$$\ln(i) = \ln(\lambda C_1 \Delta V) - (1 - \lambda)\ln(t): 0 < \lambda < 1 \quad (12)$$

For an ideal capacitor,  $\lambda = 0$ . The constant  $C_1$  is the capacitance after 1 second has passed. It is interesting to note that the solution resistance does not appear in Equation 12.

Figure 12 was obtained by plotting  $\ln(i)$  vs.  $\ln(t)$ , for each of the measured temperatures. Herein this type of plot will be referred to as an Aoki plot (ref). As time increases, the relative amount of noise increases as well. By recognizing that the slopes of these lines are  $-(1 - \lambda)$ , and the intercepts are  $\ln(\lambda C_1 \Delta V)$ , values for  $C_1$  and  $\lambda$  can easily be determined. The measured values of  $C_1$  and  $\lambda$  can be seen in Table 2.

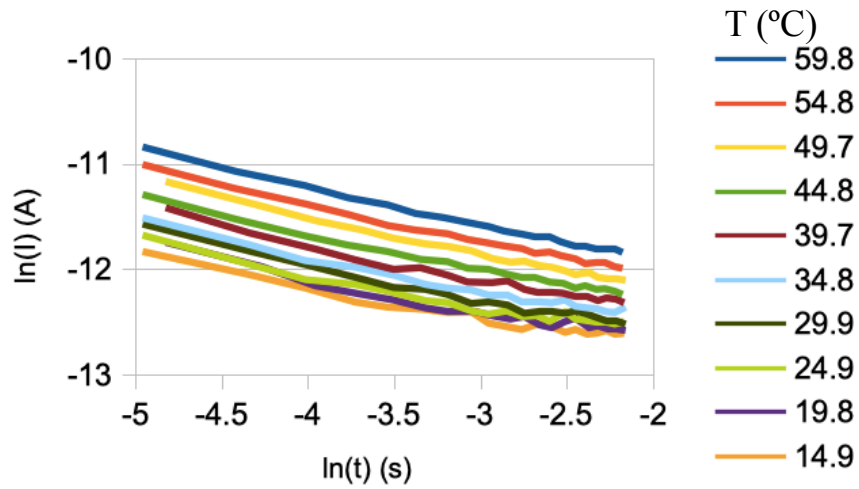


Figure 12 Aoki Plots for 200mV Pulse at Each Temperature

Table 2 LINEST results from Aoki plot.

| T (°C) | R <sup>2</sup> | m              | b               | $\lambda$     | C <sub>1</sub> (μF/cm <sup>2</sup> ) |
|--------|----------------|----------------|-----------------|---------------|--------------------------------------|
| 59.8   | 0.995          | -0.351 ± 0.006 | -12.621 ± 0.019 | 0.649 ± 0.003 | 338 ± 2                              |
| 54.8   | 0.993          | -0.340 ± 0.007 | -12.739 ± 0.021 | 0.660 ± 0.004 | 304 ± 2                              |
| 49.7   | 0.992          | -0.342 ± 0.007 | -12.867 ± 0.022 | 0.658 ± 0.005 | 275 ± 3                              |
| 44.8   | 0.990          | -0.320 ± 0.008 | -12.942 ± 0.024 | 0.680 ± 0.005 | 251 ± 3                              |
| 39.7   | 0.971          | -0.311 ± 0.013 | -13.016 ± 0.039 | 0.689 ± 0.005 | 233 ± 3                              |
| 34.8   | 0.973          | -0.302 ± 0.012 | -13.09 ± 0.04   | 0.698 ± 0.007 | 214 ± 3                              |
| 29.9   | 0.973          | -0.316 ± 0.012 | -13.22 ± 0.04   | 0.684 ± 0.008 | 204 ± 3                              |
| 24.9   | 0.947          | -0.279 ± 0.016 | -13.17 ± 0.05   | 0.721 ± 0.008 | 196 ± 3                              |
| 19.8   | 0.939          | -0.285 ± 0.017 | -13.24 ± 0.05   | 0.715 ± 0.008 | 190 ± 3                              |
| 14.9   | 0.955          | -0.269 ± 0.014 | -13.25 ± 0.04   | 0.731 ± 0.008 | 184 ± 3                              |

C<sub>1</sub> increases with temperature. If C<sub>1</sub> is proportional to the rate of dielectric excitation, this is expected (why? need some elaboration). Values for  $\lambda$  show that the capacitance strays far from ideal behavior, and that the excitation process should have a large effect on the behavior of the system.(what other process could have the effects?)

### SECTION 4.3 CHRONOAMPEROMETRY OF FERRICYANIDE UNDER KINETIC CONTROL

After data concerning the 0.1 M KCl background was collected, the solution was swapped with the 2.98 mM solution of potassium ferricyanide ( $\text{K}_3[\text{Fe}(\text{CN})_6]$ ). As before, the Haake recirculating bath was initially set to 65°C and allowed to cool to 10°C. Every 5°, two chronoamperometry experiments were performed. The parameters for the two experiments were the same as described for those done on the KCl background solution. Data for the chronoamperometry experiments under diffusion controlled conditions will be discussed in Chapter 5. Here, the data obtained under kinetic controlled conditions is presented.

The chronoamperograms were processed after subtracting the capacitive background. No averaging or smoothing was performed. The background-subtracted chronoamperograms for the ferricyanide solution under diffusion control are shown in Figure 13. The magnitude of current falls as temperature rises, which implies that the reaction is endothermic. A higher gain setting would have greatly reduced the level of noise present in this data.

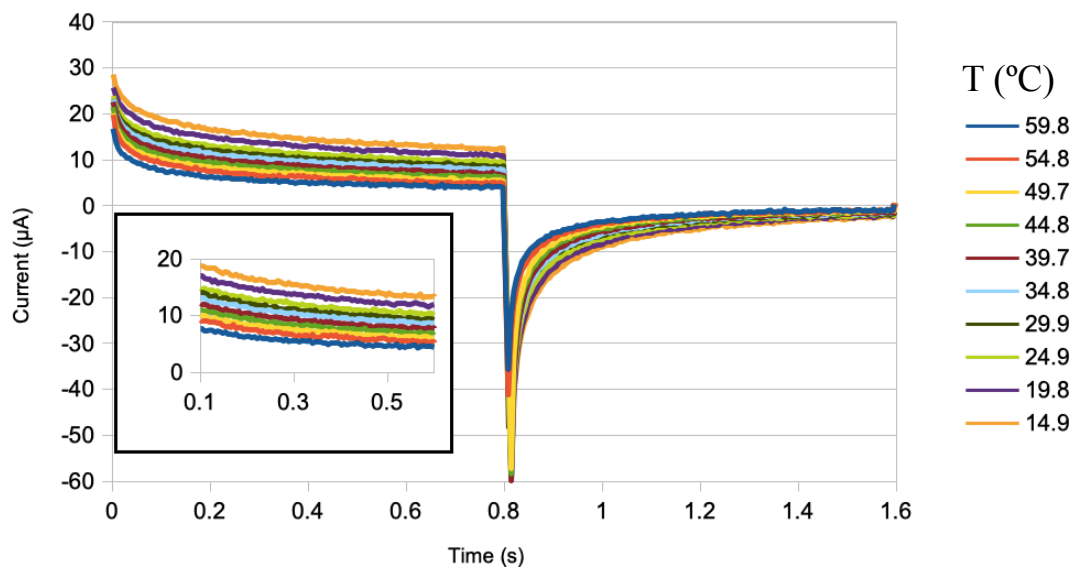


**Figure 13 KCl background subtracted Chronoamperograms of Potassium Ferricyanide Under Kinetic Control: 400-200 mV Pulse.**

Through integration using the trapezoid rule, corresponding chronocoulograms were produced. These are shown in Figure 14. Just as the observed currents decrease with an increase in temperature, so do the charges,  $Q$ . The noise-reducing effect of integration is apparent here.

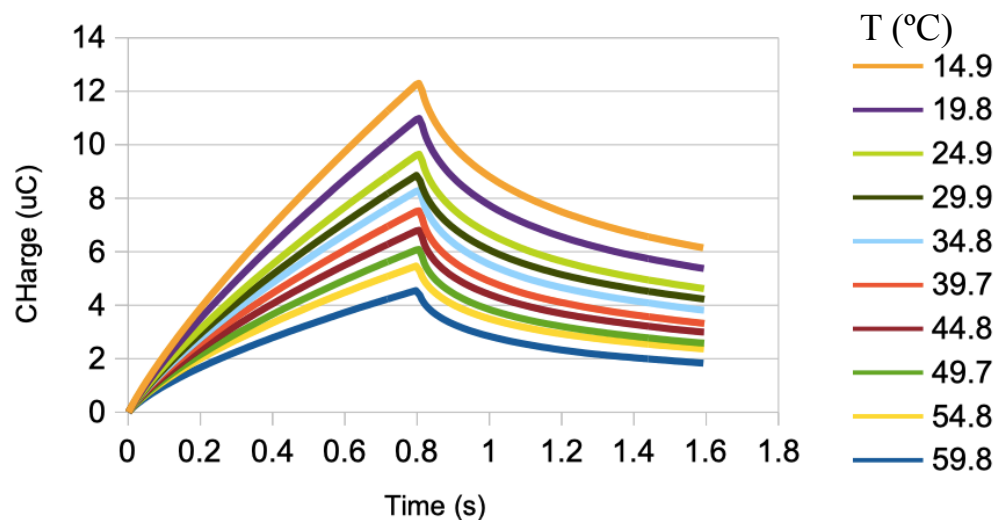


Figure 14 Chronocoulograms of Potassium Ferricyanide Under Kinetic Control.

According to Equation 7, the charge should vary linearly as a function of  $t^{1/2}$ . Plotting  $Q$  vs.  $t^{1/2}$  for each chronocoulogram gives Figure 15. The linearity assumption appears to break down somewhat at lower temperatures. The rule of thumb is that linearity holds at times such that  $t^{1/2} > 5/H$ , where  $H$  is inversely proportional to  $t_i^{1/2}$ . If linear regression is performed on the segments shown in Figure 15,  $t_i^{1/2}$  increases with temperature due to the increasing rate. This drives  $H$  to be smaller, and therefore increases the amount of time needed before the curve becomes linear. Nevertheless, the curves are linear enough to work with.

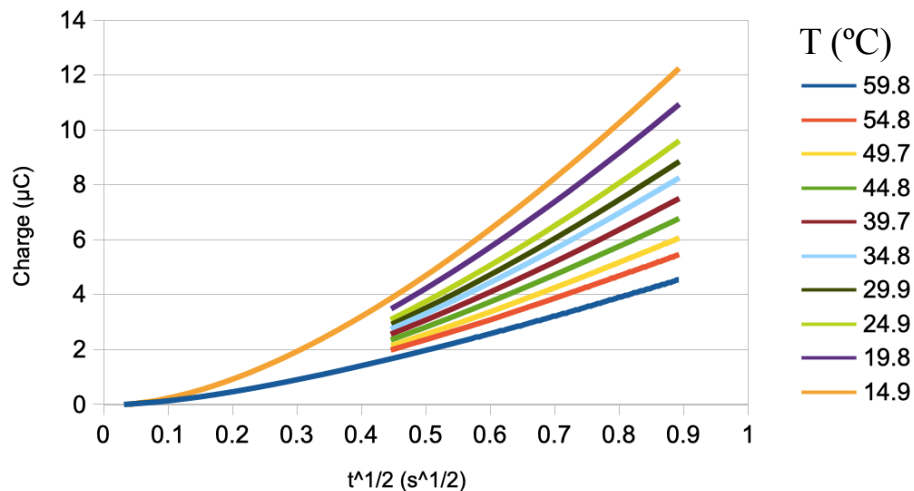


Figure 15 Q vs  $t^{1/2}$  at Various Temperatures from Kinetics Data.

#### SECTION 4.4 DETERMINATION OF HETEROGENOUS ELECTRON TRANSFER RATE

#### CONSTANTS, ELECTRON TRANSFER ACTIVATION ENERGY, AND FREQUENCY FACTOR

The heterogenous electrons transfer rate constants calculated by way of linear regression on the portion of the data from  $t^{1/2} = 0.45$  to  $0.90$  are shown in Table 3. The calculated  $k$  value of  $1.94 \times 10^{-3}$  cm/s at  $25^\circ\text{C}$  is comparable to what has been reported for similar systems<sup>13</sup> and are consistent with the ferri/ferrocyanide system being quasi-reversible. The  $\ln(k)$  was plotted as a function of reciprocal temperature, known as an Arrhenius plot, is shown in Figure 16. The slope of this line is  $-E_a/R$ , as implied by Equation 8. Likewise, the intercept is  $\ln(A)$ . The grey data point was omitted from the regression.

**Table 3 Results for k at each Temperature.**

| T (°C) | $k_f \cdot 10^{-3}(\text{cm/s})$ |
|--------|----------------------------------|
| 59.8   | $1.07 \pm 0.01$                  |
| 54.8   | $1.28 \pm 0.01$                  |
| 49.7   | $1.36 \pm 0.01$                  |
| 44.8   | $1.49 \pm 0.02$                  |
| 39.7   | $1.61 \pm 0.02$                  |
| 34.8   | $1.72 \pm 0.02$                  |
| 29.9   | $1.82 \pm 0.02$                  |
| 24.9   | $1.94 \pm 0.02$                  |
| 19.8   | $2.18 \pm 0.03$                  |
| 14.9   | $2.43 \pm 0.03$                  |

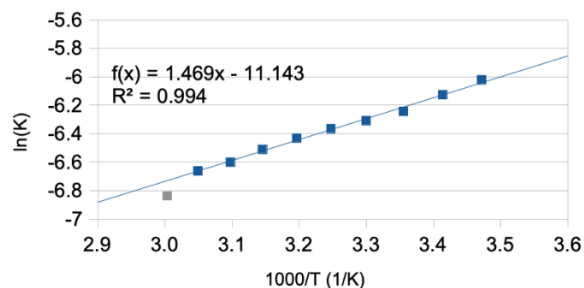


**Figure 16 Arrhenius Plot.**

The positive slope seen in Figure 16 implies a negative activation energy. Electron transfer from GCE to ferricyanide is believed to take place via an inner-sphere mechanism<sup>14-16</sup>. This means ferricyanide ion must adsorb to the surface of the electrode before electron transfer can take place. Adsorption is an exothermic process and is analogous to a particle falling into a potential energy well. Increasing the temperature increases the number of ions with sufficient energy to both stay out of the well and escape before electron transfer occurs, in turn lowering the reaction rate. The electron transfer activation energy and frequency factor were calculated to be  $-12.2 \pm 0.4$  kJ/mol and  $(1.5 \pm 0.2) \times 10^{-5}$  cm/s, respectively. To the best of our knowledge, these two important parameters are reported here for the first time.

## **CHAPTER 5: CHRONOAMPEROMETRY OF POTASSIUM FERRICYANIDE UNDER DIFFUSION CONTROL**

### **SECTION 5.1 MEASUREMENT OF THE CAPACITIVE BACKGROUND**

As previously stated, the capacitive responses of the 0.1 M KCl solution to the larger pulses from 400 mV to -200 mV were also taken as recirculating bath cooled. The resulting chronoamperograms are seen in Figure 17. The observed capacitive currents again increase with temperature. The currents are significantly higher than those measured under the larger pulse; this is congruous with the fact that the potential step is three times larger. The SNR ratio is likewise much higher, and signals in the expanded view appear significantly cleaner.

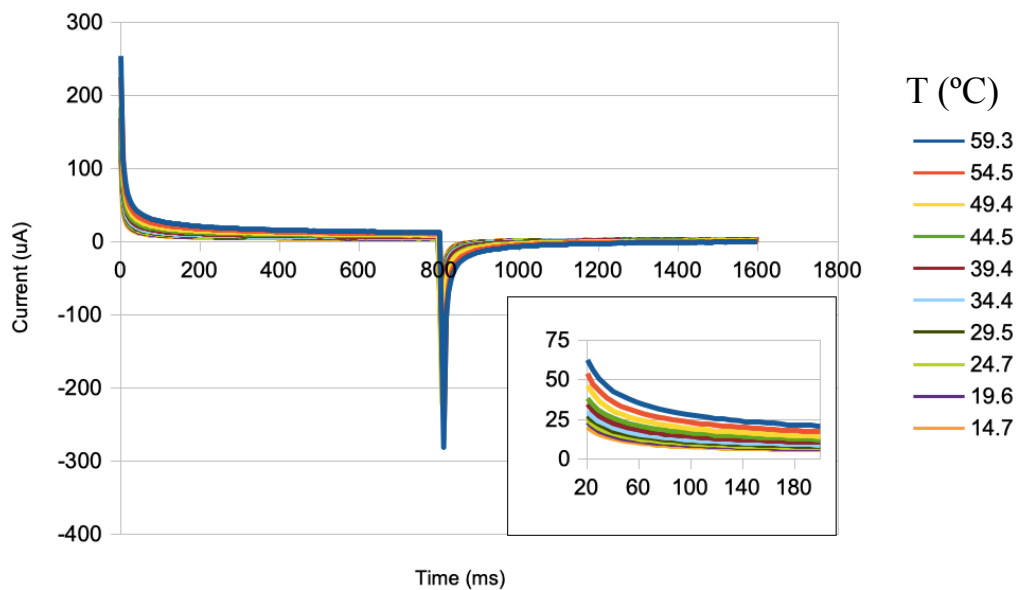


Figure 17 Chronoamperograms of aqueous KCl. Pulse: 400 mV to -200 mV vs. SSC

As before, the curves can be linearized using Equation 12. The linear portions of the resulting Aoki plots can be seen in Figure 18. As  $\ln(t)$  increases, the noise appears to increase. At lower temperatures, data deviates slightly from linearity. A higher gain setting might change this. The LINEST results, as well as the results of calculating both  $\lambda$  and  $C_1$  are shown in Table 4.

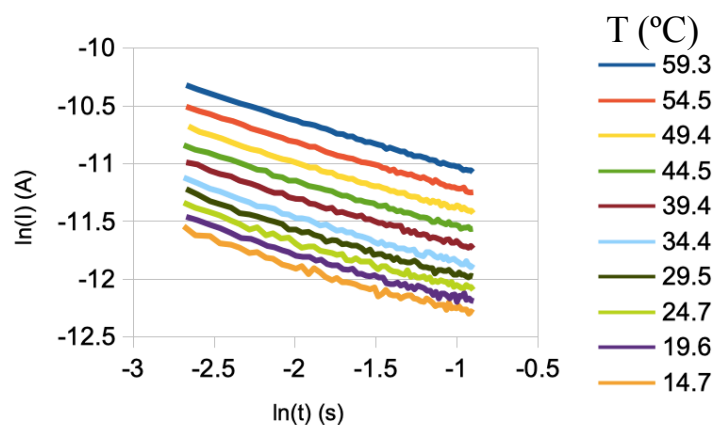


Figure 18 Aoki Plots. KCl 400 mV to -200 mV

Table 4 Regression Results from 400 mV to -200 mV Aoki Plot

| T (°C) | R <sup>2</sup> | m              | b               | $\lambda$     | C <sub>1</sub> (μF/cm <sup>2</sup> ) |
|--------|----------------|----------------|-----------------|---------------|--------------------------------------|
| 59.3   | 0.999          | -0.414 ± 0.002 | -11.448 ± 0.003 | 0.586 ± 0.002 | 368 ± 2                              |
| 54.5   | 0.997          | -0.410 ± 0.003 | -11.626 ± 0.004 | 0.590 ± 0.003 | 306 ± 2                              |
| 49.4   | 0.996          | -0.407 ± 0.003 | -11.797 ± 0.006 | 0.593 ± 0.003 | 256 ± 2                              |
| 44.5   | 0.996          | -0.404 ± 0.003 | -11.951 ± 0.005 | 0.596 ± 0.003 | 218 ± 2                              |
| 39.4   | 0.995          | -0.409 ± 0.004 | -12.109 ± 0.006 | 0.591 ± 0.004 | 188 ± 2                              |
| 34.4   | 0.992          | -0.409 ± 0.005 | -12.27 ± 0.01   | 0.591 ± 0.005 | 160 ± 2                              |
| 29.5   | 0.991          | -0.411 ± 0.005 | -12.38 ± 0.01   | 0.589 ± 0.005 | 144 ± 2                              |
| 24.7   | 0.988          | -0.401 ± 0.006 | -12.47 ± 0.01   | 0.599 ± 0.006 | 129 ± 2                              |
| 19.6   | 0.987          | -0.398 ± 0.006 | -12.57 ± 0.01   | 0.602 ± 0.006 | 117 ± 2                              |
| 14.7   | 0.982          | -0.389 ± 0.007 | -12.66 ± 0.01   | 0.611 ± 0.007 | 105 ± 2                              |

The calculated values for  $\lambda$  again indicate that a constant capacitance does not represent the double layer capacitance in this system accurately, giving supporting evidence for why a standard exponential decay should fit the data poorly. The general trend of C<sub>1</sub> increasing as a function of temperature is seen again. The values of both  $\lambda$  and C<sub>1</sub> should remain constant with respect to the size of the potential step. Plotting C<sub>1</sub> vs. temperature for both the small and large pulses yields Figure 19. Although the curves do not overlap entirely, they are relatively close. The general trend of increasing C<sub>1</sub> with

temperature is consistent with theory (ref?). As temperature increases, dipoles within the solution have more energy on average to overcome the energy barrier required to align themselves with the electric field. This causes the dielectric constant to increase more rapidly, and in turn raises  $C_1$ .

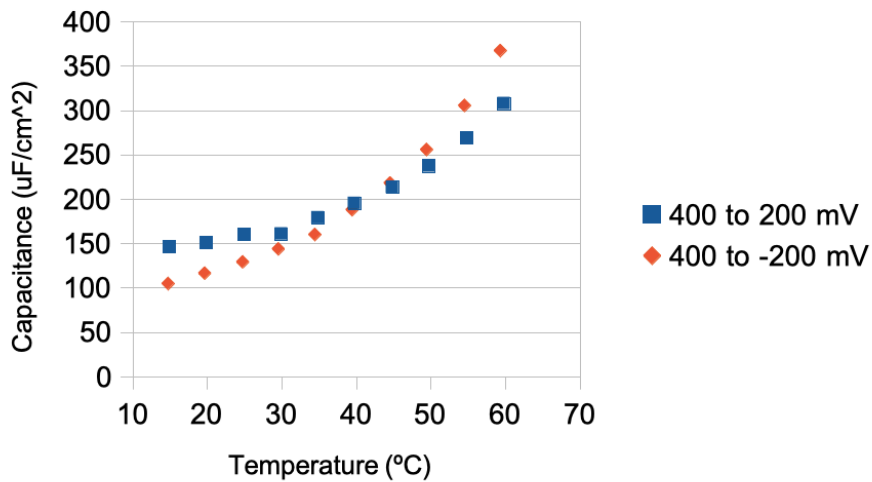


Figure 19  $C_1$  vs T at Different Potential Steps.

## SECTION 5.2 CHRONOAMPEROMETRY OF POTASSIUM FERRICYANIDE UNDER DIFFUSION CONTROLLED CONDITIONS

The background-subtracted chronoamperograms for ferricyanide taken under diffusion control can be seen in Figure 20. These exhibit the largest amount of current of all the experiments and have very low noise. Under diffusion control, the current apparently increases with temperature. This is to be expected; increasing the temperature increases the thermal motion of the ions in solution, making it easier for them to diffuse.

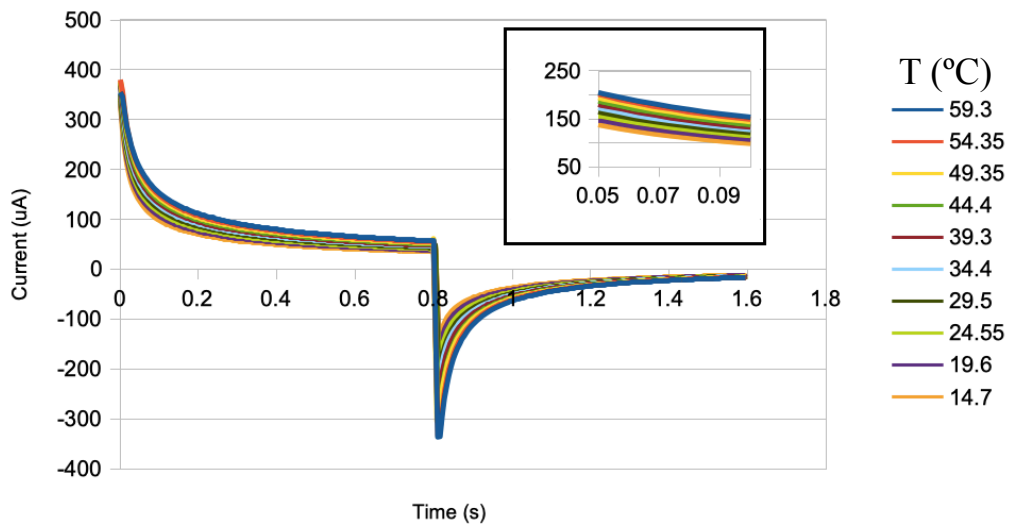


Figure 20 Chronoamperograms of Potassium Ferricyanide Under Diffusion Control

Again, by using the trapezoid rule, the chronoamperograms can be integrated to produce corresponding chronocoulougrams, seen in Figure 21.

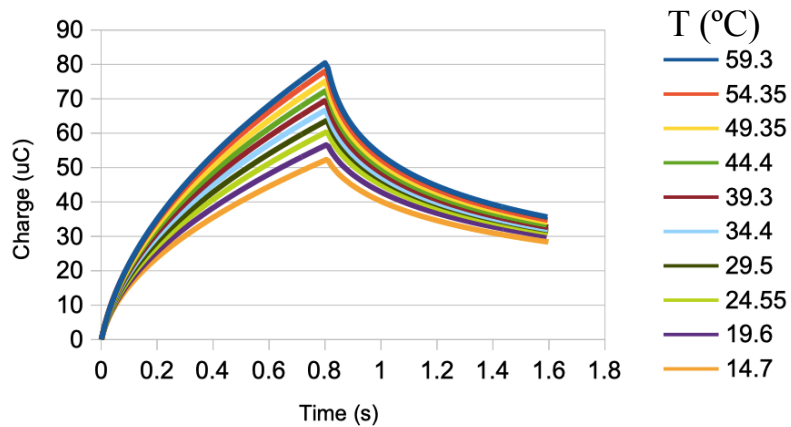


Figure 21 Chronocoulougrams of Ferricyanide Under Diffusion Control

### SECTION 5.3 DETERMINATION OF DIFFUSION COEFFICIENTS AND IONIC MOBILITY

By plotting  $Q$  vs  $t^{1/2}$  for the forward pulse, the chronocoulograms are linearized. The Cottrell plots are shown in Figure 22. Data from the entire forward pulse was plotted for the highest and lowest temperatures, but only the linear portion is shown for the remaining temperatures. If linear regression is performed on the linear portions of the data, the slopes of these lines allow for the determination of the diffusion constant for ferricyanide at each temperature, according to the Cottrell equation. The intercepts in principle can be used to calculate the surface excess. However, the upwards concavity at early times indicates that, at least briefly, the reaction is still slightly kinetically controlled at this potential. The upward concavity forces the intercepts to be negative.

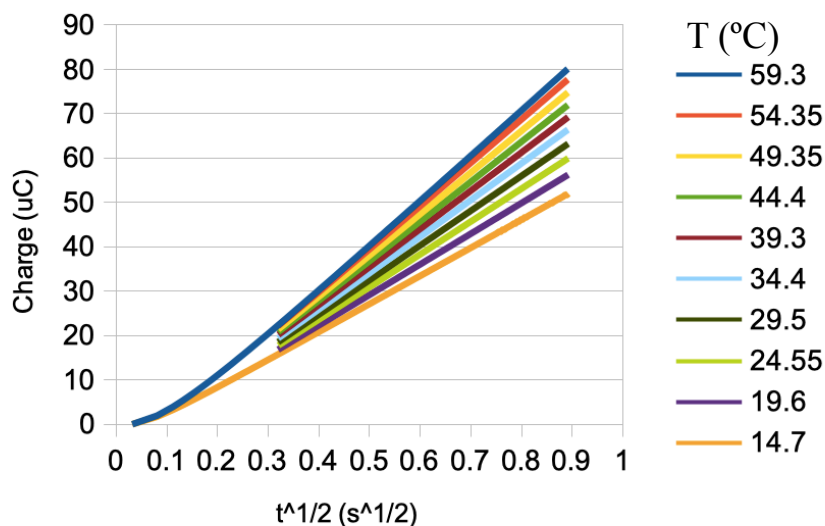
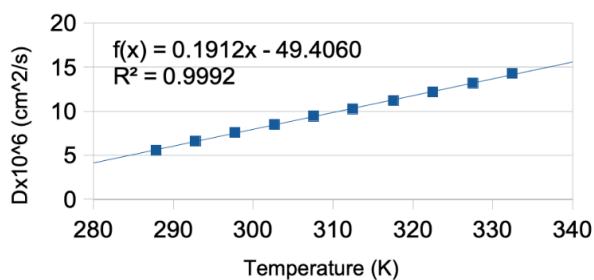


Figure 22 Cottrell Plots of Potassium Ferricyanide. Forward Pulse: 400 to -200 mV vs. SSC

To calculate the diffusion constants at different temperatures, first the effective area of the electrode had to be determined. The electrode was a 3 mm GCE. The effective area was expected to be slightly higher than its geometric area of  $7.1 \times 10^{-2} \text{ cm}^2$ , because even a small amount of surface roughness adds to the overall surface area. The diffusion constant of ferricyanide at  $25^\circ\text{C}$  is reported<sup>10</sup> to be  $7.60 \times 10^{-6} \text{ cm}^2 \text{ s}^{-1}$ . The slope of the Cottrell plot at  $25^\circ\text{C}$  is  $78.87 \pm 0.02 \text{ cm}^2 \text{ s}^{-3/2}$ . By the Cottrell equation, the effective electrode area is  $(8.26 \pm 0.02) \times 10^{-2} \text{ cm}^2$ . This area was then used to calculate the diffusion constants at the rest of the temperatures studied. The constants are listed below in Table 5, as well graphically in Figure 23 with temperature converted to Kelvin.

**Table 5 Calculated Diffusion Coefficients**

| <b>T (°C)</b> | <b>D <math>10^6(\text{cm}^2/\text{s})</math></b> |
|---------------|--------------------------------------------------|
| 59.3          | $14.31 \pm 0.01$                                 |
| 54.4          | $13.21 \pm 0.01$                                 |
| 49.4          | $12.191 \pm 0.009$                               |
| 44.4          | $11.196 \pm 0.009$                               |
| 39.3          | $10.278 \pm 0.007$                               |
| 34.4          | $9.451 \pm 0.007$                                |
| 29.5          | $8.515 \pm 0.006$                                |
| 24.6          | 7.60                                             |
| 19.6          | $6.617 \pm 0.004$                                |
| 14.7          | $5.581 \pm 0.003$                                |



**Figure 23 Linear Regression of D vs. T**

As temperature increases, the diffusion constant appears to increase linearly. The slope of the regression in Figure 23 should be equal to the product  $\mu k_B/q$  according to the Einstein-Smoluchowski equation. Multiplying the slope by  $k_B/q$ , the ionic mobility was

calculated to be  $(2.22 \pm 0.02) \times 10^{-3} \text{ cm}^2 \text{ s}^{-1} \text{ V}^{-1}$ . The ionic mobility of ferricyanide at infinite dilution has been reported<sup>10</sup> to be  $1.047 \times 10^{-3} \text{ cm}^2 \text{ s}^{-1} \text{ V}^{-1}$ . The linearity seen in Figure 23 suggests that ionic mobility varies little with temperature over this range (any explanation?).

Plotting  $\ln(D)$  vs.  $1/T$  results in the Arrhenius plot seen in Figure 24. The negative slope implies that diffusion is an endothermic process, which satisfies intuition; a molecule must take up energy to move. The activation energy for diffusion is calculated to be  $16.2 \pm 0.5 \text{ kJ/mol}$ . This is comparable with that reported in literature via voltammetry (or viscosity??) of  $17 \pm 1 \text{ kJ/mol}$  in sodium hydroxide supporting electrolyte<sup>17</sup>. The frequency factor obtained from the intercept is  $(5 \pm 1) \times 10^3 \text{ cm}^2/\text{s}$ . The agreements between two completely different techniques validates the measurement.

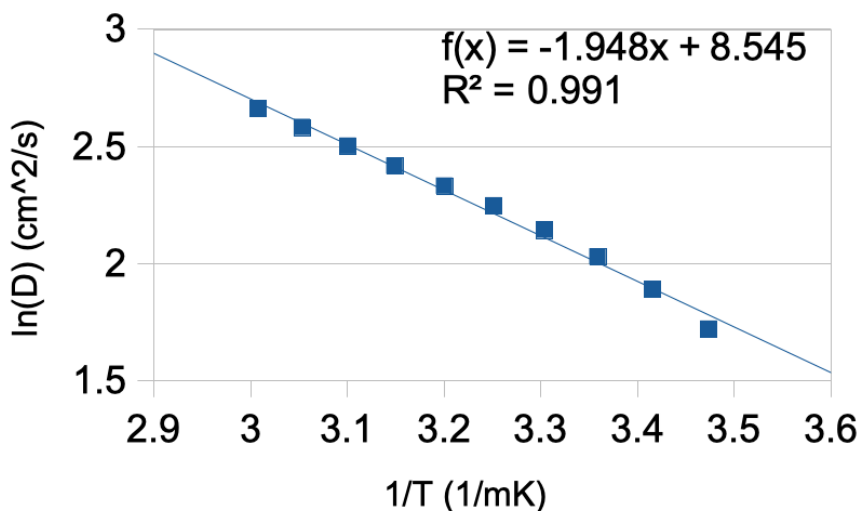


Figure 24 Arrhenius plot for the Diffusion of Ferricyanide

## SECTION 5.4 ANALYSIS OF THE REVERSE PULSE AND MEASUREMENT OF SURFACE EXCESS

The reverse pulse chronocoulogram can be linearized by plotting  $q$  vs.  $\theta$  according to Equation 5. The results are shown in Figure 25. As done with the forward pulse, all the data for the highest and lowest temperatures is shown. Only the linear section of the plots ( $0.3 < t^{1/2} < 0.52$ ) was used for regression.

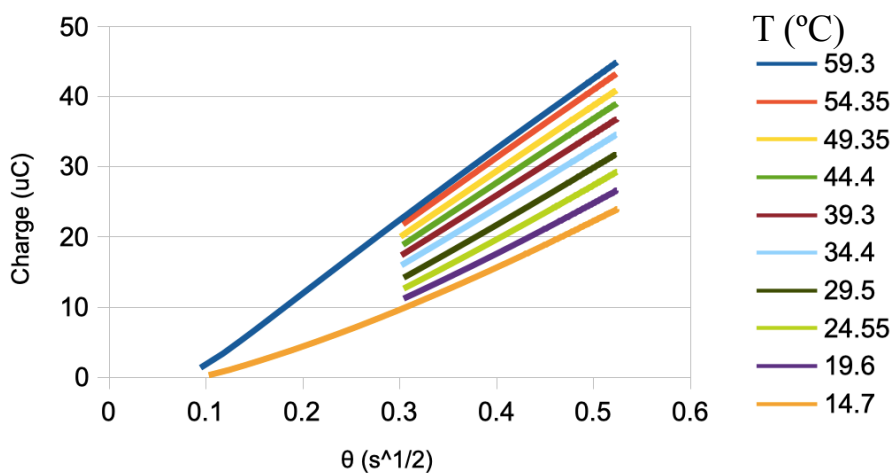


Figure 25 Linearized Reverse Pulse for Ferricyanide Under Diffusion Control

To calculate the diffusion constants using the reverse pulse data, the electrode area was taken to be the same as measured from the forward pulse. Then, using Equation 5, each of the diffusion constants were calculated. The results are provided in Table 6, along with the percent difference when compared to those obtained at the same temperature using the forward pulse. With the exception of those calculated for the two highest temperatures, the diffusion constants measured using the reverse pulse are higher than those using the

forward pulse. Figure 26 shows the same data along with a linear regression.

Table 6 Diffusion Constants from Reverse Pulse

| T (°C) | D 10 <sup>6</sup> (cm <sup>2</sup> /s) | % Difference |
|--------|----------------------------------------|--------------|
| 59.3   | 13.89 ± 0.02                           | 2.94         |
| 54.4   | 13.11 ± 0.01                           | 0.74         |
| 49.4   | 12.217 ± 0.008                         | 0.21         |
| 44.4   | 11.580 ± 0.006                         | 3.37         |
| 39.3   | 10.654 ± 0.006                         | 3.59         |
| 34.4   | 9.866 ± 0.012                          | 4.30         |
| 29.5   | 9.072 ± 0.018                          | 6.33         |
| 24.6   | 8.075 ± 0.024                          | 6.06         |
| 19.6   | 6.964 ± 0.028                          | 5.11         |
| 14.7   | 5.827 ± 0.028                          | 4.32         |

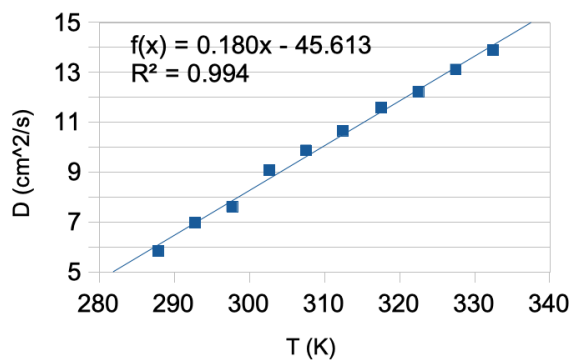
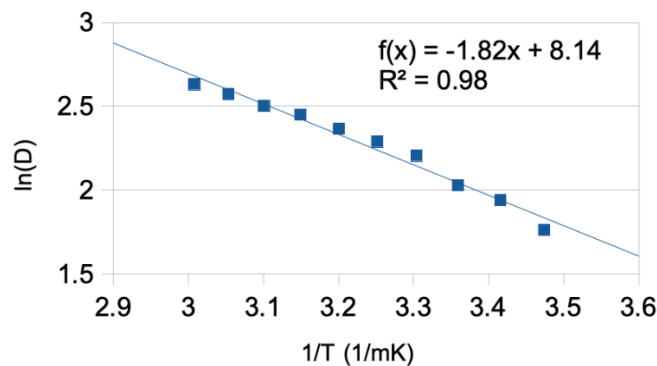


Figure 26 D vs. T. Reverse Pulse

The slope of the regression is multiplied by  $k_B/q$  to calculate the ionic mobility. The value obtained from the reverse pulse data was  $2.05 \pm 0.05 \text{ cm}^2 \text{ s}^{-1} \text{ V}^{-1}$ , which is comparable to that from the forward pulse. As before,  $\ln(D)$  vs.  $1/T$  produces a linear plot, seen in Figure 27. From the slope and intercept, the activation energy and frequency factor were calculated to be  $14.8 \pm 0.8 \text{ kJ/mol}$  and  $3 \pm 1 \text{ cm}^2/\text{s}$  respectively. The activation energy calculated is smaller than that from the forward pulse. This can be traced back to the fact that the diffusion constants were mostly higher at the same temperatures.



**Figure 27 Reverse Pulse Arrhenius Plot for Diffusion.**

Even though the surface excess of ferricyanide cannot be directly determined, the difference between that of ferricyanide and ferrocyanide can be determined because the difference in the intercepts of Equations 4 and 5 is just  $nFA(\Gamma_O - \Gamma_R)$ . The difference in the intercepts of the linearized chronocoulograms for the forward and reverse pulse was calculated for each temperature. The difference in the surface excess  $\Gamma_O - \Gamma_R$  is plotted as a function of temperature in Figure 27. Below  $\sim 46^\circ\text{C}$ , the surface concentration of ferricyanide is higher. Above, it is the surface concentration of ferrocyanide that is higher. At temperatures below  $25^\circ\text{C}$ , the difference deviates from linearity.

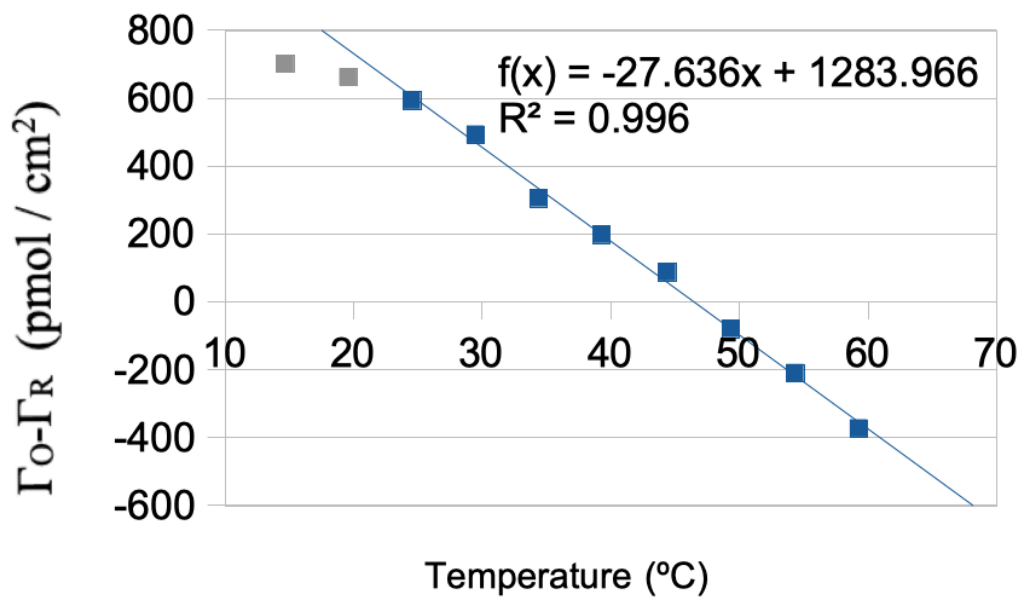


Figure 28  $\Gamma_{O}-\Gamma_{R}$  as a function of Temperature.

## CHAPTER 6: CONCLUSIONS

### SECTION 6.1 DESIGN SUCCESSES AND POTENTIAL IMPROVEMENTS

An Arduino shield potentiostat with 0.5 mV potential control and the ability to measure currents from 10 nA to 5 mA was designed and fabricated. The range of the potential range of the potentiostat in a three-electrode configuration is  $\pm 3.3$  V, which covers the whole electrochemical window. In a two-electrode configuration, it easily goes to  $\pm 4.5$  V. This makes it the highest resolution microcontroller-based potentiostat known to the author with respect to potential. The maximum ramp rate is comparable to those achieved by other potentiostats, as discussed in the introduction. The circuit also exhibits very high SNR ( $>1000$ ) when the proper CVC gain is used.

Like with most microcontroller-based potentiostats, the maximum ramp rates and sampling rates is fairly low. The biggest limiting factor for this is printing the data to the screen as it is being collected. Furthermore, with the limited memory available on the Arduino, this has to be done this way. Even CV experiments sweeping over small potential ranges exceeds the Arduino's available memory space. This could easily be fixed by the addition of an SPI memory chip to the potentiostat. Preliminary tests suggest that ramp rates could be improved dramatically (easily up to 5000 mV/s) with 2 mV resolution and 10000 mV/s with 4 mV resolution.

Two of the gain settings available to the CVC did not function as intended. This

was due to the type of digital switch that was used. A multiplexer would be a better choice, as they are available with significantly smaller leakage currents. With some calibration, this should allow for the measurements of currents down to about 10 pA.

Higher quality operational amplifiers would improve the design in a few ways. First, a smaller offset voltage would decrease calibration issues. Larger potentials might also be available in a three-electrode system. It might also help reduce the ripple present in the voltage source.

## **SECTION 6.2 POTENTIOSTAT PERFORMANCE**

The potentiostat appears to function very well for such a simple circuit. The circuit has low noise and provides accurate results when tested on dummy-cells. It is notable that the CV of a capacitor assumes the box shape is a validation of a good circuit performance. The shape becomes more distorted and noisier as the value of the capacitance decreases. This could be improved by increasing the gain or through additional filtering of the signals entering the ADC.

Because an electrochemical cell behaves a lot like an RC circuit, accurate results when chronoamperometry was performed on such a circuit is a good indicator of the circuit functioning properly. The time-constant measured was in full agreement with that calculated by measuring the values of the components.

## **SECTION 6.3 TEMPERATURE DEPENDENT ELECTROCHEMISTRY**

The potentiostat fulfilled its designed purpose. Double pulse chronoamperometry was performed under both kinetic and diffusion-controlled conditions at ten different

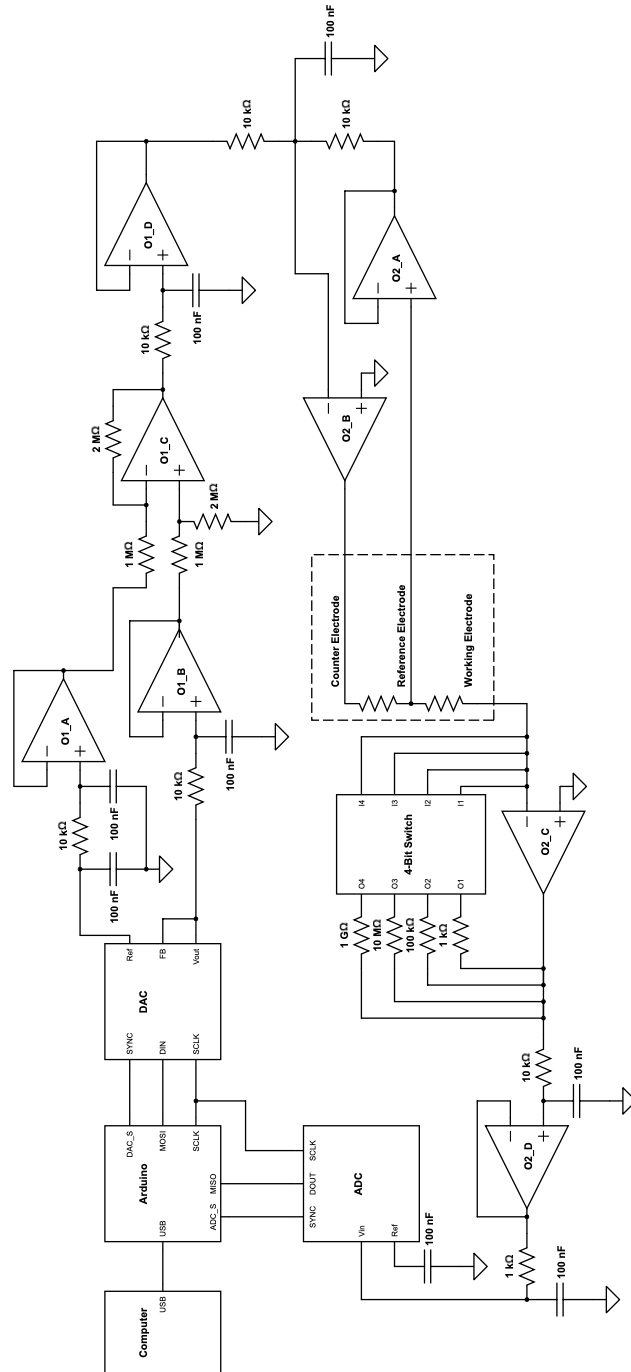
temperatures. The capacitive background of the electrolyte solution was taken under both potential steps at all the same temperatures, and the current was found to follow a power law rather than exponential decay.

Under kinetic controlled conditions, current decreased as temperature increased. The heterogeneous electron transfer rate constant for the reduction of ferricyanide on CGE was measured at each temperature. The magnitude of the rate constants is consistent with a quasi-reversible reaction. The activation energy and frequency factor were determined from this temperature dependent kinetics data. The activation energy was found to be negative. This supports the belief that ferricyanide reduction occurs via an inner-sphere mechanism.

Under diffusion control, current increased with increasing temperature. Data was used to calculate the diffusion coefficient for ferricyanide at each of the temperatures using both the forward and reverse pulse. Some difference was observed between them. The temperature dependent diffusion data was used to calculate the ionic mobility and activation energy of diffusion for ferricyanide, both of which agreed with values reported in literature. The difference in surface excess between ferricyanide and ferrocyanide as a function of temperature was observed. There is a critical temperature where the concentration of ferrocyanide becomes greater than that of ferricyanide on the electrode surface.

## **APPENDIX**

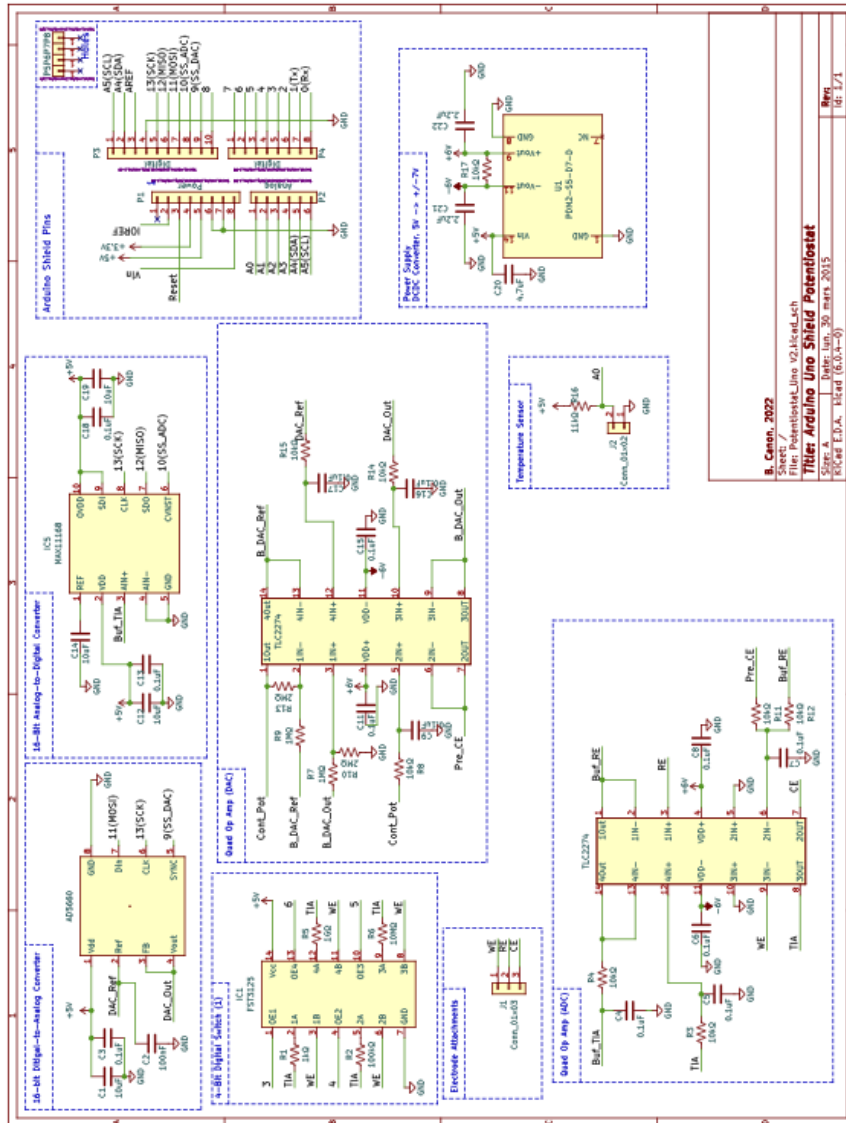
## A.1 POTENTIOSTAT SCHEMATIC



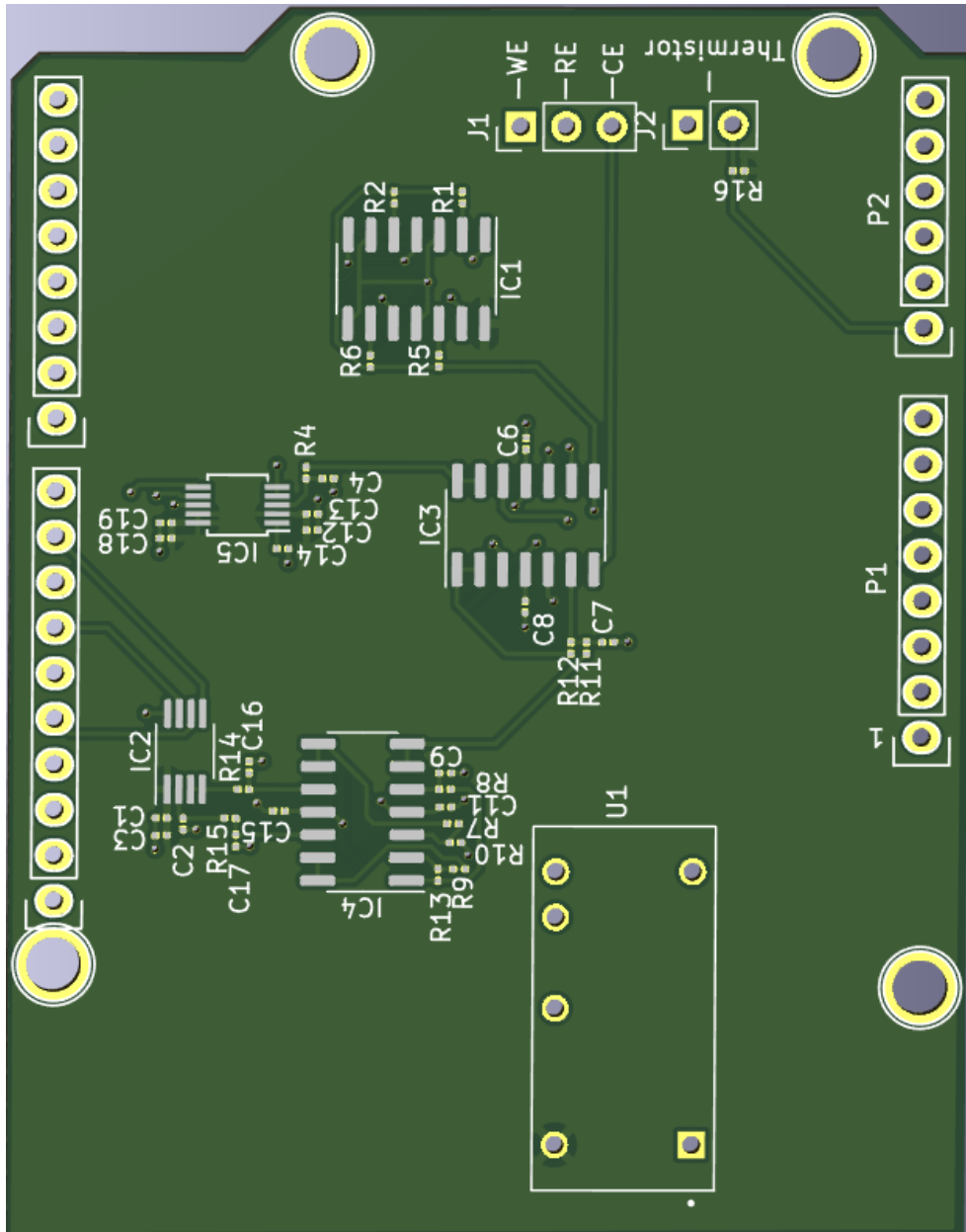
## A.2 COST BREAKDOWN

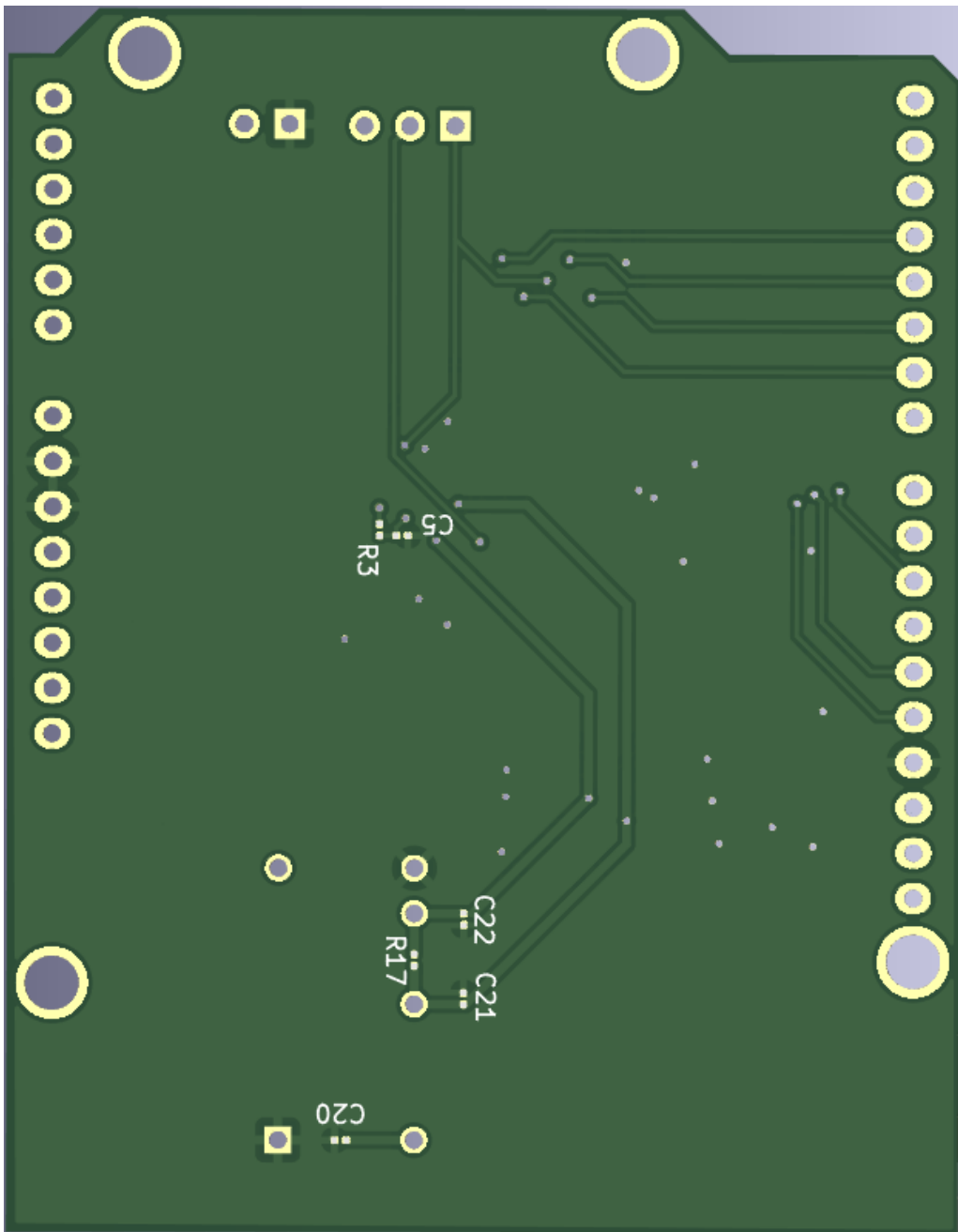
| Item                | Description             | Supplier    | Quantity | Price per Unit (USD)     | Total (USD)  |
|---------------------|-------------------------|-------------|----------|--------------------------|--------------|
| AD5660              | DAC                     | Mouser      | 1        | 11.59                    | 11.59        |
| MAX11168            | ADC                     | Mouser      | 1        | 29.80                    | 29.80        |
| TLC2274             | Quad Op-Amp             | Mouser      | 2        | 2.87                     | 5.74         |
| FST3125             | 4b Digital Switch       | Mouser      | 1        | 0.67                     | 0.67         |
| C0603X5R1E104K030BB | 0.1 $\mu$ F Capacitor   | Mouser      | 13       | 0.10                     | 1.30         |
| GRM155R60J106ME15D  | 10 $\mu$ F Capacitor    | Mouser      | 4        | 0.17                     | 0.68         |
| 02016D475MAT2A      | 4.7 $\mu$ F Capacitor   | Mouser      | 2        | 0.40                     | 0.80         |
| 0201ZD225MAT2A      | 2.2 $\mu$ F Capacitor   | Mouser      | 1        | 0.48                     | 0.48         |
| CRCW02011K00FNED    | 1 k $\Omega$ Resistor   | Mouser      | 2        | 0.12                     | 0.24         |
| CRCW020110K0FNED    | 10 k $\Omega$ Resistor  | Mouser      | 6        | 0.12                     | 0.72         |
| CRCW020111K0FNED    | 11 k $\Omega$ Resistor  | Mouser      | 1        | 0.12                     | 0.12         |
| CRCW0201100KFKED    | 100 k $\Omega$ Resistor | Mouser      | 1        | 0.28                     | 0.28         |
| CRCW02011M00FKED    | 1 M $\Omega$ Resistor   | Mouser      | 2        | 0.28                     | 0.56         |
| CRCW02012M00FNED    | 2 M $\Omega$ Resistor   | Mouser      | 2        | 0.12                     | 0.24         |
| CRCW020110M0FNED    | 10 M $\Omega$ Resistor  | Mouser      | 1        | 0.12                     | 0.12         |
| PDM2-S5-D7-D        | DC-DC Converter         | DigiKey     | 1        | 8.16                     | 8.16         |
| LS-00004            | Break Away Headers      | Microcenter | 37       | 0.03                     | 1.11         |
| PCB Board           | PCB                     | JLCPCB      | 1        | 0.40                     | 0.40         |
|                     |                         |             |          | <b>Grand Total (USD)</b> | <b>63.01</b> |

### A.3 KiCAD COMPONENT SCHEMATIC

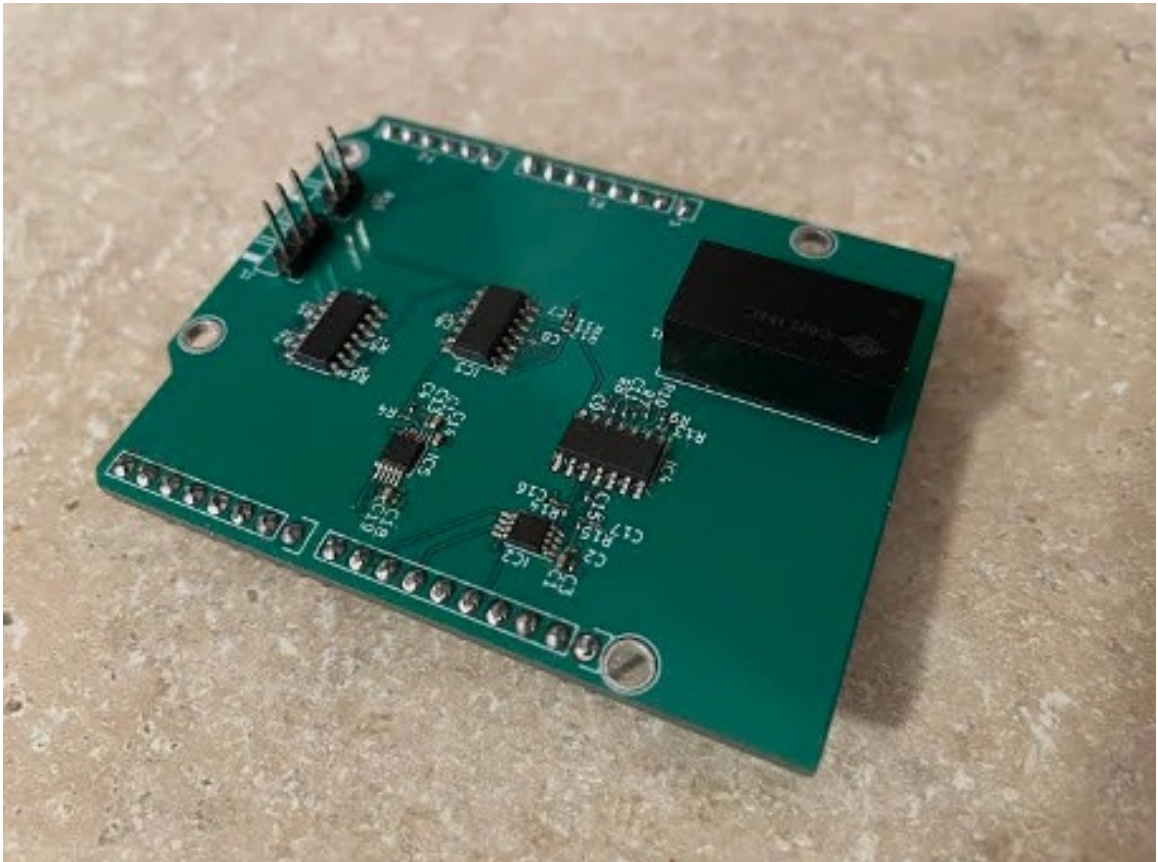


## A.4 KICAD PCB LAYOUT





## A.5 POTENTIostat SHIELD



## REFERENCES

1. Jin, H.; Qin, Y.; Pan, S.; Alam, A. U.; Dong, S.; Ghosh, R.; Deen, M. J. Open-Source Low-Cost Wireless Potentiometric Instrument for PH Determination Experiments. *J. Chem. Educ.* **2018**, *95* (2), 326–330. <https://doi.org/10.1021/acs.jchemed.7b00479>.
2. Arrizabalaga, J. H.; Simmons, A. D.; Nollert, M. U. Fabrication of an Economical Arduino-Based Uniaxial Tensile Tester. *J. Chem. Educ.* **2017**, *94* (4), 530–533. <https://doi.org/10.1021/acs.jchemed.6b00639>.
3. Bullis, R.; Coker, J.; Belding, J.; De Groot, A.; Mitchell, D. W.; Velazquez, N.; Bell, A.; Hall, J.; Gunderson, W. A.; Gunderson, J. E. C. The Fluorino: A Low-Cost, Arduino-Controlled Fluorometer. *J. Chem. Educ.* **2021**, *98* (12), 3892–3897. <https://doi.org/10.1021/acs.jchemed.1c00876>.
4. Meloni, G. N. 3D Printed and Microcontrolled: The One Hundred Dollars Scanning Electrochemical Microscope. *Anal. Chem.* **2017**, *89* (17), 8643–8649. <https://doi.org/10.1021/acs.analchem.7b01764>.
5. Meloni, G. N. Building a Microcontroller Based Potentiostat: A Inexpensive and Versatile Platform for Teaching Electrochemistry and Instrumentation. *J. Chem. Educ.* **2016**, *93* (7), 1320–1322. <https://doi.org/10.1021/acs.jchemed.5b00961>.
6. Li, Y. C.; Melenbrink, E. L.; Cordonier, G. J.; Boggs, C.; Khan, A.; Isaac, M. K.; Nkhonjera, L. K.; Bahati, D.; Billinge, S. J.; Haile, S. M.; Kreuter, R. A.; Crable, R. M.; Mallouk, T. E. An Easily Fabricated Low-Cost Potentiostat Coupled with

- User-Friendly Software for Introducing Students to Electrochemical Reactions and Electroanalytical Techniques. *J. Chem. Educ.* **2018**, *95* (9), 1658–1661.  
<https://doi.org/10.1021/acs.jchemed.8b00340>.
7. Rajendran, S. T.; Scarano, E.; Bergkamp, M. H.; Capria, A. M.; Cheng, C.-H.; Sanger, K.; Ferrari, G.; Nielsen, L. H.; Hwu, E.-T.; Zór, K.; Boisen, A. Modular, Lightweight, Wireless Potentiostat-on-a-Disc for Electrochemical Detection in Centrifugal Microfluidics. *Anal. Chem.* **2019**, *91* (18), 11620–11628.  
<https://doi.org/10.1021/acs.analchem.9b02026>.
  8. Glasscott, M. W.; Verber, M. D.; Hall, J. R.; Pendergast, A. D.; McKinney, C. J.; Dick, J. E. SweepStat: A Build-It-Yourself, Two-Electrode Potentiostat for Macroelectrode and Ultramicroelectrode Studies. *J. Chem. Educ.* **2020**, *97* (1), 265–270. <https://doi.org/10.1021/acs.jchemed.9b00893>.
  9. Brown, E. W.; Glasscott, M. W.; Conley, K.; Barr, J.; Ray, J. D.; Moores, L. C.; Netchaev, A. ACEstat: A DIY Guide to Unlocking the Potential of Integrated Circuit Potentiostats for Open-Source Electrochemical Analysis. *Anal. Chem.* **2022**, *94* (12), 4906–4912. <https://doi.org/10.1021/acs.analchem.1c04226>.
  10. Bard, A. J.; Faulkner, L. R. *Electrochemical Methods: Fundamentals and Applications, 2nd Edition*; John Wiley & Sons, Incorporated, 2000.
  11. Anson, F. C. Innovations in the Study of Adsorbed Reactants by Chronocoulometry. *Anal. Chem.* **1966**, *38* (1), 54–57.  
<https://doi.org/10.1021/ac60233a014>.

12. Aoki, K. J.; Chen, J.; He, R. Potential Step for Double-Layer Capacitances Obeying the Power Law. *ACS Omega* **2020**, *5* (13), 7497–7502.  
<https://doi.org/10.1021/acsomega.0c00301>.
13. Blaedel, W. J.; Engstrom, R. C. Investigations of the Ferricyanide-Ferrocyanide System by Pulsed Rotation Voltammetry. *Anal. Chem.* **1978**, *50* (3), 476–479.  
<https://doi.org/10.1021/ac50025a030>.
14. Chen, Piehong.; Fryling, M. A.; McCreery, R. L. Electron Transfer Kinetics at Modified Carbon Electrode Surfaces: The Role of Specific Surface Sites. *Anal. Chem.* **1995**, *67* (18), 3115–3122. <https://doi.org/10.1021/ac00114a004>.
15. Chen, P.; McCreery, R. L. Control of Electron Transfer Kinetics at Glassy Carbon Electrodes by Specific Surface Modification. *Anal. Chem.* **1996**, *68* (22), 3958–3965. <https://doi.org/10.1021/ac960492r>.
16. Daum, P. H.; Enke, C. G. Electrochemical Kinetics of the Ferri-Ferrocyanide Couple on Platinum. *Anal. Chem.* **1969**, *41* (4), 653–656.  
<https://doi.org/10.1021/ac60273a007>.
17. Gross, M.; Jordan, J. Voltammetry at Glassy Carbon Electrodes. **1984**, *56* (8), 1095–1129. <https://doi.org/10.1351/pac198456081095>.

## **BIOGRAPHY**

Benjamin Canon received his Bachelor of Science in Chemistry from George Mason University in 2018. From there, he went on to work for the Department of Homeland Security. After receiving his Master of Science in Chemistry, he will continue to serve the public.